Chapter 3

Electromagnetics for Quantitative Magnetic Resonance Imaging*

Stephen E. Russek[†,§], Karl F. Stupic[†], Joshua R. Biller[†], Michael A. Boss[†], Kathryn E. Keenan[†], and Elizabeth Mirowski[‡]

[†]*Physical Measurement Laboratory, NIST, Boulder, Colorado 80305, USA*

[‡]*High Precision Devices, Boulder, Colorado 80301, USA*

[§]stephen.russek@nist.gov

Magnetic resonance imaging (MRI) is based on radio frequency (RF) interrogation of the human body at frequencies between 40 and 300 MHz. An RF transmitter excites proton spin precession and then, in a manner analogous to an RF identification tag, the proton's precessional ring down reports back local information about its environment. Here, we introduce the use of MRI as a quantitative measurement tool that employs electromagnetic (EM) transmit and receive channels to non-invasively probe inside objects such as the human body. Understanding the propagation of RF into the human body and how to manipulate and detect the nuclear spin probes provide methods to obtain quantitative measurements of local tissue properties and disease states. We present Bloch simulations describing how RF and magnetic gradient pulses can be used to control and manipulate nuclear spin dynamics and show how quantitative information can be obtained from MRI. We show how standard phantoms (imaging calibration structures) can be used to assess accuracy and variability of MRI-based measurements. We review MRI RF transmit and receive systems, measurement of the local proton relaxation times, the effect of complex EM material properties on images and MRI-based measurement of EM properties of complex materials (e.g., living humans).

Contents

3.1. Quantitative MRI

3.1.1. *Introduction*

Magnetic resonance imaging (MRI) is a spatially resolved form of nuclear magnetic resonance (NMR) where nuclear spins are excited and detected using radio frequency (RF) magnetic fields.[1–3] *The purpose of this chapter is to introduce the use of MRI as a quantitative measurement tool that employs electromagnetic (EM) transmit and receives channels to noninvasively probe inside objects such as the human body.* A brief introduction to the physics of the nuclear spin resonance will be given, followed by a description of the

Bloch equations, which provide a numerical framework to understand and calculate nuclear spin dynamics, as the spins interact with static, gradient, and RF magnetic fields. Next, we review how RF and magnetic field gradient pulses can be used to encode the spatial location of the spins, as well as information on the local environment around the spins. An introduction to some of the simpler MRI transmit and receive systems will be presented. The remainder of the chapter will then focus on using different pulse sequences to make quantitative image-based measurements and methods to verify their accuracy using calibration structures referred to as phantoms. The goal of transforming MRI into a precise noninvasive *in vivo* metrology is motivated by the need for medical imaging to provide more comprehensive, reliable, and objective information to guide improved diagnosis and treatment.

Most clinical MRI systems excite and detect the proton spin resonance, which has a precessional frequency given by $f_0 = \frac{\gamma_p}{2\pi} B_0$, where B_0 is the static magnetic field and $\frac{\gamma_p}{2\pi} = 42.577\ 478\ 518(18)\,\mathrm{MHz/T}$ is the proton gyromagnetic ratio divided by 2π. For clinical MRI systems, the most common magnetic field strengths are 1.5 and 3.0 T with 7 T systems coming online. The corresponding resonance frequencies are 63.9, 127.7, and 298 MHz, respectively. Most imaging is done by interrogating water protons, since they have a very high concentration in the human body (body average $\sim$65 mol/L), and, due to their rapid motion, they have narrow linewidths. Other protons, notably those on fats, metabolites, and neurotransmitters can also be observed and identified by their chemical shift. Chemical shift refers to the down-shift of the proton spin resonance frequency, for a given applied magnetic field, due to the diamagnetic response of the surrounding electron orbitals, which reduces the field at the nucleus. For water, at 25°C and a spherical sample geometry, there is a fractional down-shift of 25.691×10^{-6} in the resonant frequency relative to that of a bare proton.[4]

Proton spins are exquisite subatomic probes for *in vivo* measurements. They are high-Q resonators whose resonant frequency and relaxation times are sensitive to their microscopic surroundings. Relative precessional frequencies can be precisely determined by measuring the phase shifts of spin packets in different regions of the image. Relative phase differences below $\Delta\varphi = 0.1$ rad can be detected, which, for a resonant frequency of $f_0 = 128\,\mathrm{MHz}$ and an interrogation time of $\Delta t = 100\,\mathrm{ms}$, give a frequency sensitivity of $\frac{\Delta\phi}{2\pi f_0 \Delta t} = 1.2 \times 10^{-9}$. Part per billion (ppb) frequency shifts can be detected, allowing proton spins to probe their local chemical environment, small differences in tissue magnetic susceptibilities or local temperature. Chemical shifts are on the order of a few parts per million (ppm). Protons in $-CH_2-$ and $-CH_3-$ groups in fats have typical fractional chemical

shifts of 3.35×10^{-6} and 3.75×10^{-6}, respectively, of the resonant frequency relative to that of water protons. Variation in tissue magnetic susceptibilities $\Delta\chi$,[a] which can be as large as $\Delta\chi = 1.0 \times 10^{-6}$ to 2.1×10^{-6} for deoxygenated/oxygenated blood,[5] can give rise to local field variations of the same order of magnitude. The proton resonant frequency may also be temperature-dependent. For water protons in a spherical sample, the frequency shift is $-10.36(30) \times 10^{-9\circ}\mathrm{C}^{-1}$ over the range 5–45°C.[4]

While the local environment can change proton spin resonant frequencies by several ppm, it can change the proton spin relaxation times by many orders of magnitude. For an isolated proton in a magnetic field, the intrinsic lifetime is given by the inverse of the dipole relaxation rate $\frac{1}{W} = 6\pi c^3/\mu_0\gamma_p^2\hbar\omega^3 \approx 10^{22}\,\mathrm{s}$, for a frequency of $\frac{\omega}{2\pi} = 120\,\mathrm{MHz}$, where c is the speed of light, μ_0 is the permeability of free space, and $\hbar$ is the reduced Planck constant.[6] For a proton in thermal equilibrium with a bath of photons at body temperature in a resonator with $Q = 100$ and a volume about the size of a body coil, the relaxation time is on the order of 10^{14} s. For an ensemble of proton spins interacting with surrounding tissue, the proton spin relaxation times are much shorter, seconds to microseconds. Table 3.1 lists typical tissue spin relaxation time values.

The proton magnetization vector is given by $\mathbf{M}(\boldsymbol{r}, t) = \frac{\sum_i \langle \boldsymbol{\mu_i} \rangle}{V_s}$, where $\langle \boldsymbol{\mu_i} \rangle$ is the expectation value of the magnetic moment of the ith proton in the volume V_s at a point $\boldsymbol{r}$. In general, the sum is over all MRI-visible protons, which is mainly protons in unbound water molecules. Although all protons contribute to the nuclear magnetization, protons bound to large, more-rigid molecules tend to have short relaxation times and are not visible on conventional NMR/MRI measurement time scales. Proton density (PD)[7] is defined as the ratio, in percent, of MRI-visible protons to the proton concentration of pure water at 37°C (see Table 3.1 for typical tissue values). At a given location in a tissue, the PD may be composed of many different spin packets.[b] For example, in white matter, we may have spin packets that represent the water trapped in myelin layers, cytoplasmic water and extracellular water. $\mathbf{M}(t)$ is a vector quantity, and assuming axial symmetry, there are two important relaxation times, T_1 and T_2. T_1 is the longitudinal relaxation time, the exponential time constant required for the nuclear magnetization to relax

[a] All quantities reported in this chapter are given in SI units.

[b] A spin packet, often referred to as an isochromat, refers to an ensemble of like spins, which is spatially large on the atomic scale, but small on the scale of the variations in local magnetic fields. Spins are alike if they belong to the same species, are in the same chemical environment, and are in the same structural environment, e.g., they are all flowing together. We prefer the use of "spin packet" to isochromat, since isochromat originally referred to spins with the same Larmor frequency and we are generalizing to similar spins sharing a similar environment.

Table 3.1. Typical proton density (PD), T_1, and T_2 for tissues at 1.5 and 3 T and approximately 37°C.

Tissue	PD (%)	T_1@ 1.5 T (ms)	T_2@ 1.5 T (ms)	T_1 @ 3 T (ms)	T_2 @ 3 T (ms)
Blood		1441 ± 120 (Ref. 9)	290 ± 30 (Ref. 9)	1932 ± 85 (Ref. 9)	275 ± 50 (Ref. 9)
Bone marrow		288 ± 5.27 (Ref. 10)	165 ± 4.96 (Ref. 10)	365 ± 9 (Ref. 10)	133 ± 6.14 (Ref. 10)
Breast fat		296 ± 13 (Ref. 11)	53 ± 2 (Ref. 11)	366 ± 75 (Ref. 11)	53 ± 9 (Ref. 11)
Breast fibroglandular		1266 ± 82 (Ref. 11)	58 ± 10 (Ref. 11)	1445 ± 93 (Ref. 11)	54 ± 9 (Ref. 11)
Breast fibroglandular				1680 ± 180 (Ref. 12)	71 ± 6 (Ref. 12)
Cartilage		1060 ± 155 (Ref. 10)	42.1 ± 7.05 (Ref. 10)	1240 ± 107 (Ref. 10)	36.9 ± 3.81 (Ref. 10)
Cortical bone				223 ± 11 (Ref. 13)	0.39 ± 0.19 (Ref. 13)
Cerebral spinal fluid	100 (Ref. 7)	3337 (Ref. 14)	2562 (Ref. 14)	3817 ± 424 (Ref. 15)	
Cerebral spinal fluid				4522 ± 417 (Ref. 16)	
Gray matter	70 (Ref. 17)	989 ± 44 (Ref. 15)	90 ± 4 (Ref. 15)	1122 ± 117 (Ref. 15)	79 ± 5 (Ref. 15)
Gray matter	84 ± 5 (Ref. 18)	1057 ± 172 (Ref. 18)	89 ± 10 (Ref. 18)	1193 ± 65 (Ref. 19)	109 ± 11 (Ref. 19)
Kidney cortex				1142 ± 154 (Ref. 20)	76 ± 7 (Ref. 20)
Kidney medulla				1545 ± 142 (Ref. 20)	81 ± 8 (Ref. 20)
Liver				809 ± 71 (Ref. 20)	34 ± 4 (Ref. 20)
Myocardium				1159 (Ref. 21)	45 (Ref. 21)
Pancreas				725 ± 71 (Ref. 20)	43 ± 7 (Ref. 20)
Prostate				1700 ± 175 (Ref. 8)	80 ± 34 (Ref. 8)
Skeletal muscle		1130 ± 91.7 (Ref. 10)	35.3 ± 3.85 (Ref. 10)	1420 ± 38.1 (Ref. 10)	31.7 ± 1.9 (Ref. 10)
Spleen				1328 ± 31 (Ref. 20)	61 ± 9 (Ref. 20)
Subcutaneous fat		288 ± 8.42 (Ref. 10)	165 ± 5.5 (Ref. 10)	371 ± 7.94 (Ref. 10)	133 ± 4.43 (Ref. 10)
Synovial fluid		2850 ± 279 (Ref. 10)	1210 ± 140 (Ref. 10)	3620 ± 320 (Ref. 10)	767 ± 48.8 (Ref. 10)

(*Continued*)

Table 3.1. (*Continued*)

Tissue	PD (%)	T_1@ 1.5 T (ms)	T_2@ 1.5 T (ms)	T_1 @ 3 T (ms)	T_2 @ 3 T (ms)
Uterus cervix				1616 ± 613 (Ref. 20)	83 ± 7 (Ref. 20)
Uterus endometrium				1453 ± 123 (Ref. 20)	59 ± 1 (Ref. 20)
Uterus myometrium				1514 ± 156 (Ref. 20)	79 ± 10 (Ref. 20)
White matter	78 (Ref. 17)	616 ± 32 (Ref. 15)	92 ± 4 (Ref. 15)	758 ± 49 (Ref. 15)	81 ± 3 (Ref. 15)
White matter	66 ± 4 (Ref. 18)	637 ± 59 (Ref. 18)	76 ± 8 (Ref. 18)	781 ± 61 (Ref. 19)	65 ± 6 (Ref. 19)

Notes: For a full review of tissue properties at 3 T, the readers are referred to Bojorquez *et al.*[8] Reported tissue relaxation times from the literature can vary widely, and there is difficulty in determining how much is due to tissue variation versus measurement variation. Here, where available, we report the average and standard deviation of the data.

back to its equilibrium value along the static magnetic field direction. The most important energy term for a proton spin ensemble in a large magnetic field (assumed to be along the z-axis) is the Zeeman energy $U_Z = -\mathbf{M} \cdot \mathbf{B_0}$, which depends only on the longitudinal magnetization M_z. For T_1 relaxation, where the magnetization relaxes back to its equilibrium value along $\mathbf{B_0}$, the proton spin must irreversibly exchange energy with its environment. T_2 is the transverse relaxation time, the exponential time constant required for the precessional component of the nuclear magnetization, transverse to the static field, to relax back to zero. T_1 and T_2, which are field- and temperature-dependent, are phenomenological parameters that need careful definition to be used as biomarkers. Table 3.1 shows some typical tissue relaxation times that are relevant for and accessible to measurement by MRI.

The excitation and detection of proton spin allows for the measurement of motion of otherwise identical particles. Through the use of magnetic field gradients, one can encode spatial information into the spin degree of freedom, which can then be used to measure *in vivo* the self-diffusion of water, water flow, or more complicated motions such as tissue perfusion.

In addition to being a ubiquitous probe, proton spins can be excited by and retransmit RF radiation, which weakly interacts with the tissue. The long-RF penetration depths allow MRI to see through the human body with small perturbations to the tissue. Other parts of the EM spectrum, including microwaves, optical, and X-ray radiation interact strongly with tissue leading to either insufficient penetration or tissue damage.

In this chapter, we give an introduction to the use of MRI as a precise metrology that uses RF radiation as a probe for the quantitative *in vivo* measurement of important parameters that can then be used as biomarkers. A biomarker, per the Food and Drug Administration (FDA) definition,[22] refers to "a characteristic that is objectively measured and evaluated as an indicator of normal biological processes, pathogenic processes or biological responses to a therapeutic intervention." MRI biomarkers include local proton spin resonant frequencies, spin relaxation times, chemical environment, tissue/lesion volumes, tissue stiffness, water flow and diffusion, electrical conductivity and dielectric constant, magnetic susceptibility, temperature, and brain activity. These parameters, if carefully and rigorously defined, can then be used to noninvasively determine tissue structure and state, organ functionality, and eventually cognitive functionality.

3.1.2. *MRI signal: Bloch equations*

The power of MRI arises from the ability to precisely control and manipulate spins, which can be deeply embedded in the human body, with a combination of applied magnetic fields, magnetic field gradients, and RF pulses. The dynamics of a spin packet located at position $\mathbf{r}$ in an applied magnetic field B_0 along the z-axis are measured by monitoring the RF field produced by the proton magnetization, $\mathbf{M}(t)$, of the spin packet. We assume that the time evolution of the spin-packet magnetization is given by the Bloch equation[23]:

$$\frac{d\mathbf{M}(\mathbf{r},t)}{dt} = \gamma\mathbf{M}\times\mathbf{B} - \frac{M_z - M_0}{T_1}\hat{z} - \frac{\mathbf{M}_{xy}}{T_2}, \tag{3.1}$$

where γ is the gyromagnetic ratio (typically, $\gamma = \gamma_{wp}$ is the water proton gyromagnetic ratio), $\mathbf{B} = \mathbf{B_0}+\mathbf{B}_L+\mathbf{B}_1(t)+\mathbf{B}_n\,(t)+\mathbf{G}_z\cdot\mathbf{r}$ is the magnetic flux density for the spin packet at position $\mathbf{r}$, $\mathbf{B_0} = B_0\hat{z}$ is the macroscopic main field (defined to be along the z-axis) due to the solenoid and shim coils,[c] $\mathbf{B}_L$ is the local field produced by the sample, $\mathbf{B}_1(t)$ represents the applied time-dependent RF fields, $\mathbf{B}_n\,(t)$ is the field created by environmental and thermal noise, $\mathbf{G}_z = \boldsymbol{\nabla}B_z$ is the applied z-axis field gradient, T_1 is the longitudinal spin relaxation time, $\mathbf{M}_{xy} = M_x\hat{x} + M_y\hat{y}$ is the transverse component of the

[c]Shimming refers to homogenizing the magnetic field around the sample by placing passive magnetic shims or by using superconducting and room temperature coils. Superconducting and passive shims are implemented during the system setup to homogenize the magnetic field. Currents in room temperature shim coils are adjusted at run time to compensate for field distortions created by the sample/patient. Dynamical shimming may be used to vary the shimming during the imaging process to correct for different imaging regions. Shim coils are wound to compensate first-, second-, third-, and some fourth-order spherical harmonic distortions.

proton magnetization, and T_2 is the transverse spin relaxation time. The equilibrium proton magnetization M_0 is

$$M_0 = \frac{\hbar^2 \gamma_{wp}^2 B_0 N_p}{4 k_b T_s}, \tag{3.2}$$

where T_s is the sample temperature and N_p is the number of protons per unit volume, $\hbar$ is the reduced Planck constant, and k_b is the Boltzmann constant. For water, $M_0 = 9.3 \times 10^{-3}$ A/m at 37°C and 3 T. The B_0 field is assumed to be much larger than all other field components. For high-field MRI and NMR ($\geq$1.5 T), B_0 is at least a factor of 100 greater than the other listed field components. In the absence of any other fields, the magnetization will precess about the B_0 field at the left-handed Larmor frequency:

$$f_0 = \frac{\gamma_{wp}}{2\pi} B_0. \tag{3.3}$$

The proton magnetization vector can be manipulated by application of RF fields perpendicular to B_0 and alternating at the Larmor frequency, which is 63.9, 127.7, and 298 MHz for field values of interest (1.5, 3.0, and 7.0 T). By application of RF fields (referred to as B_1 fields), the magnetization experiences a torque causing rotation away from B_0. Applying resonant RF pulses for specific durations will cause the magnetization to rotate and thereby acquire a component in a plane transverse to B_0, where it will precess about B_0 at the Larmor frequency, enabling inductive detection of the nuclear magnetization.

The Bloch equation is phenomenological and needs to be applied carefully. It often does not apply to spin systems with spin larger than $1/2$ since, in higher spin systems, there are many excitation levels that can have different relaxation time constants. The Bloch equation does not predict important effects such as spin echoes. To model spin echoes, an ensemble of spin packets, each obeying a Bloch equation with different local parameters, is required. We refer to the model using a linear superposition of a large ensemble of spin packets, with varying properties and local fields, each obeying the Bloch equation, as the *Bloch Model*. Although T_1, which is an energy relaxation time, is well defined, T_2 is not.[23] Transverse spin relaxation can be due to either reversible spin dephasing, such as that caused by static spatial variation in field values $\mathbf{B}_0$, $\mathbf{B}_L$, or due to irreversible dephasing effects, which comprise the T_2 term. The spin dephasing rate, $1/T_2^*$, is the sum of these two terms[3,23]:

$$\frac{1}{T_2^*} = \frac{1}{T_2'} + \frac{1}{T_2}. \tag{3.4}$$

The first term, $1/T_2'$, is usually thought of as extrinsic dephasing process; the second term, $1/T_2$, as intrinsic dephasing process. The distinction between the extrinsic and intrinsic dephasing processes is not unique, and an operational definition of T_2 is required.

3.1.3. *Bloch solvers*

It is straightforward to numerically integrate the Bloch equations for a variety of applied RF fields and gradients.[24–26] A large ensemble of spin packets is required to mimic a real system that can contain 10 moles of proton spins in an imaging slice. Each spin packet is chosen to represent a large ensemble of similar spins with sufficient size such that the thermal magnetization noise can be ignored. It is convenient to calculate the system in a rotating frame of reference, which is rotating clockwise around the z-axis, when viewed from above the origin, with a frequency $\omega_{\rm rot}$ near the resonance frequency. Going to a rotating reference frame mathematically means that $B_0\hat{z} \rightarrow (B_0 - \omega_{\rm rot}/\gamma)\hat{z}$ and the frequency of clockwise circularly polarized applied RF fields are reduced by $\omega_{\rm rot}$, whereas the counterclockwise polarized RF fields have the frequencies increased by $\omega_{\rm rot}$. For linear polarized RF fields, we will ignore the counterclockwise component. The dynamical equations then have only small frequency components that are easier to numerically calculate. The mathematical simplification of going to a rotating frame near the resonance frequency is mirrored in NMR/MRI data acquisition by mixing the observed RF signal with a precise reference at a user-defined observe frequency. All dynamical equations will be in the rotating frame unless otherwise specified.

In the case of no RF fields and a constant z-axis field B_0, the Bloch equation can be solved to give

$$M_z(t) = M_{zi} + (M_0 - M_{zi})(1 - e^{-\frac{t}{T_1}}), \tag{3.5}$$

$$M_{xy}(t) = M_{xy0}e^{-i\Delta\omega t}e^{-\frac{t}{T_2}},$$

where M_{zi} is the initial magnetization,

$$M_{xy} = M_x + iM_y;\ \Delta\omega = \gamma B_0 - \omega_{\rm rot}. \tag{3.6}$$

These equations describe precessional relaxation back to the equilibrium value of the magnetization and are referred to as free induction decays (FIDs). An example of single spin packet relaxation is shown in Fig. 3.1(a). Here, the longitudinal and transverse magnetization relax back with time constants $T_1 = 200\,\text{ms}$ and $T_2 = 100\,\text{ms}$, respectively. For an ensemble of spin packets that all have different local fields, the transverse relaxation will be faster, characterized by a time T_2^*, as shown in Fig. 3.1(b). Here, there is a 10-mm long ensemble of 10,000 spin packets with a linear distribution of local fields giving a gradient of $G_z = 0.1\,\text{mT/m}$. The insets show the real part of the Fourier transform (spectrum) of the complex transverse

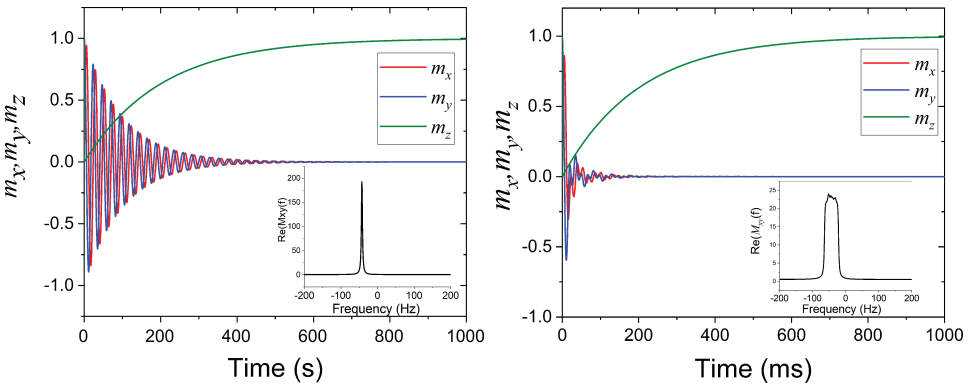

Fig. 3.1. (a) Free induction decay (FID) of a single spin packet with $T_1 = 200\,\text{ms}$, $T_2 = 100\,\text{ms}$. (b) FID of an ensemble of spin packets with a gradient of $0.1\,\text{mT/m}$ applied. The insets show the real part of the Fourier transform of the FID.

magnetization, $m_{xy}(f)$.[d] For a single spin packet, the Fourier transform of a decaying exponential gives a Lorentzian with a full width at half maximum (FWHM) of $\Delta f = \frac{1}{\pi T_2} = 3.185\,\text{Hz}$. For the distribution of spin packets in a field gradient, $m_{xy}(f)$ gives the spatial distribution of spins, which in this case, is a rectangular distribution with a bandwidth of $\frac{\gamma}{2\pi} G_z \times 10\,\text{mm} = 42.6\,\text{Hz}$.

For a Bloch simulator, when the fields are constant and one is only interested in a value after a time Δt, we can use matrix propagators[27] (which is equivalent to numerical integration in the limit of $\Delta t \to 0$):

$$\mathbf{M}(\mathbf{r},\, t + \Delta t) = R_z(\theta_g) R_{zi}(\theta_i) R_{\text{re}} R_{\text{RF}} \mathbf{M}(\mathbf{r}, t) + M_0 \left(1 - e^{-\frac{\Delta t}{T_1(r)}}\right) \hat{z}, \quad (3.7)$$

where R_z is a z-axis rotation matrix and θ_g and θ_i are the rotation angles due to the gradients and local field variations, respectively.

$$R_z = \begin{pmatrix} \cos(\theta) & \sin(\theta) & 0 \\ -\sin(\theta) & \cos(\theta) & 0 \\ 0 & 0 & 1 \end{pmatrix}, \quad (3.8)$$

$$\theta_g = \gamma \mathbf{r} \cdot \int_t^{t+\Delta t} \mathbf{G}_z(\tau) d\tau, \quad (3.9)$$

$$\theta_i = \gamma \Delta B(\mathbf{r}) \Delta t. \quad (3.10)$$

[d]In this chapter, we use lower case $m = M/M_s$ to denote normalized magnetization and the independent variable, e.g., t or f, to denote Fourier transform pairs. We refer to the time domain data as FIDs or echoes, whereas the Fourier transforms are referred to as spectra.

The rotation due to magnetic field gradients can be characterized by a time-dependent wave vector $\theta_g = \mathbf{k}(t) \cdot \mathbf{r}$, where the wave vector $\mathbf{k}(t) = \gamma \int_0^t \mathbf{G}_z(\tau) d\tau$. The ability to impose well-defined phase gradients across a sample is the basis of the most common type of spatial encoding, as discussed in the spatial encoding section.

R_{re} is the matrix that implements, along with the inhomogeneous term in Eq. (3.7), the relaxation of the magnetization

$$R_{\text{re}} = \begin{pmatrix} e^{-\frac{\Delta t}{T_2(\boldsymbol{r})}} & 0 & 0 \\ 0 & e^{-\frac{\Delta t}{T_2(\boldsymbol{r})}} & 0 \\ 0 & 0 & e^{-\frac{\Delta t}{T_1(\boldsymbol{r})}} \end{pmatrix}. \tag{3.11}$$

Unlike the precessional term, which gives rise to rotations that preserve magnetization magnitude and relative angles, the relaxation term changes the magnitude of the magnetization and describes a phenomenological coupling to a heat bath.

R_{RF} is a matrix that accounts for application of an RF field near resonance, which will be described in Section 3.1.4. Bloch simulators can use a combination of numerical integration, matrix propagators, or other types of propagators within one pulse sequence depending on the type and complexity of the applied fields.

3.1.4. *Excitation and detection of precessing spins*

To excite spins with resonant frequency Ω, RF pulses, with clockwise polarization and frequency near resonance, are applied. For an RF pulse with an amplitude B_1, a base angular frequency ω_1 and a phase ϕ,[e] going to the rotating frame of reference, the dynamical equations are equivalent to a moment precessing around a static field with a transverse component B_1 and a longitudinal component $\Delta B = (\Omega - \omega_1)/\gamma$, describing off-resonance (see Fig. 3.2). If the off-resonance field is zero and the RF pulse is applied for a time Δt, then the rotation matrix is given by

$$R_{\text{RF}} = R_z(\phi) R_x(\alpha) R_z(-\phi), \tag{3.12}$$

where R_x is a rotation about the x-axis in the rotating frame, $\alpha = \gamma B_1 \Delta t$ is the flip angle. The flip angle describes the change in the angle relative to the z-axis and hence energy transfer from the RF field to the spin system.

[e]The phases of both the RF fields and spin precession are defined relative to a stable reference oscillator. Here, we use a convention that 0°, 90°, 180°, and 270° RF pulses correspond to rotations around the $x, y, -x$, and $-y$ directions in the rotating frame, respectively.

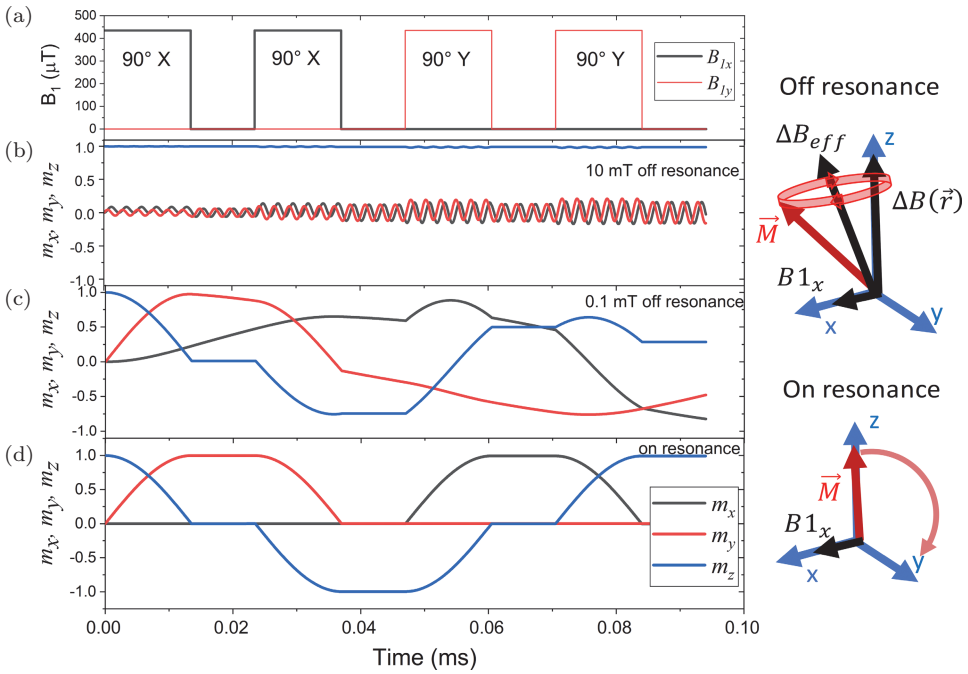

Fig. 3.2. Magnetization response, calculated using a Bloch simulator, of a spin packet, with $T_1 = 20$ ms, $T_2 = 10$ ms, for a simple pulse sequence, shown in frame (a), consisting of two 90° radio frequency (RF) pulses along x and then along y with 0.01 ms delays in between RF pulses. (b) The applied RF is far off-resonance. (c) The applied RF is off-resonance by 0.1 mT. (d) The RF is on-resonance.

If the RF radiation is applied continuously, the magnetization will precess continuously about B_1, oscillating between high- and low-energy configurations, analogous to a single spin undergoing Rabi oscillations. Most NMR and MRI systems use pulsed excitations, and typical RF pulse durations and field amplitudes are 5 μs, 500 μT for NMR and 5 ms, 50 μT for MRI.

When there is a sizeable off-resonance component, $\Delta B > B_1$ (Fig. 3.2(b)) the magnetization will precess along the combined field $\mathbf{B}_{\text{eff}} = \Delta\mathbf{B} + \mathbf{B}_1$, which, in this case, will be predominantly along the z-axis, and there will be little energy transfer from the applied RF field. When there is a small off-resonance component (Fig. 3.2(c)), the tip angle will be reduced and given by

$$\alpha = \gamma_{\text{wp}} B_{\text{eff}} \Delta t;\ B_{\text{eff}} = \sqrt{\Delta B^2 + B_1^2}. \tag{3.13}$$

For the case shown in Fig. 3.2(c), the flip angle is 88.4°, compared to 90° on-resonance.

For real systems, e.g., humans, there will be variations in local fields and RF amplitudes. Field variations occur due to imperfect shimming and variations in local magnetic susceptibility of the sample or tissue. RF variations occur due to the transmit radiation pattern and RF absorption of the sample or tissue. A nutation experiment is a method of characterizing these nonidealities and calibrating the RF amplitude. A nutation experiment applies a series of RF pulses, varying either the pulse amplitude or pulse time, to systematically increase the flip angle. The magnitude of the FID response is measured, usually by taking the peak or integrated area of the spectra. Figure 3.3 shows the NMR nutation data, signal versus RF pulse duration, for a small spherical sample and a long capillary that have good RF uniformity and poor RF uniformity, respectively. For an ideal system, one would see sinusoidal oscillations. For a real system with a distribution of local field values and RF amplitudes, it is impossible to rotate all of the

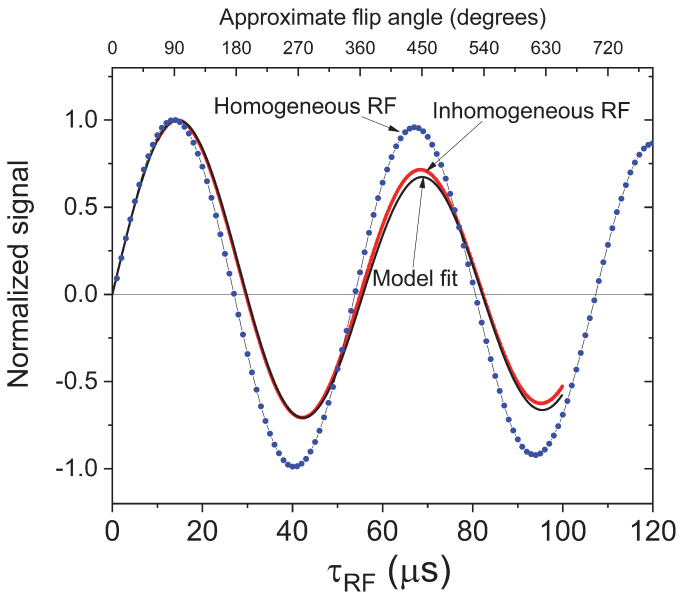

Fig. 3.3. Nutation experiments: Nuclear magnetic resonance (NMR) signal versus RF pulse duration for $CuSO_4$ water solutions showing oscillations as the radio frequency (RF) pulse duration varies from 0 to 120 μs (flip angle varies from 0° to ∼810°). The experiment is a simple RF excitation using a rectangular pulse and recording of the subsequent free induction decay (FID), as shown in Fig. 3.1. The blue curve is for a small 3-mm diameter spherical sample that has a relatively homogenous B_1 field. The red curve is for the same solution, but for a long sample that extends beyond the homogenous region of the transmit coil and, hence, has larger B_1 inhomogeneity. The black curve is a fit to the data assuming a B_1 inhomogeneity consistent with the saddle coil used for NMR transmit/receive circuit.

spins uniformly, leading to loss of polarization and signal. The damping of the sinusoid is a measure of the degree of nonuniformity. The long capillary sample data are fit (black line) with a simple model that includes RF nonuniformity consistent with the known radiation pattern of the RF saddle coil in the NMR probe, showing that most of the attenuation of the oscillations, in this case, can be attributed to B_1 inhomogeneity.

Nutation data are used to calibrate RF power and pulse duration and are required to obtain the desired flip angle. It is important to remember that there is always a distribution of flip angles in a real system/sample.

The physical parameter measured in NMR and MRI is the oscillating transverse magnetization. The detected signal is the voltage induced in a coil. The coil voltage is a linear superposition of the signal coming from all of the spin packets in a volume V. For a system where the transmit and receive coils are the same, the law of reciprocity gives the detected voltage V_{coil}[3]:

$$V_{\text{coil}} = \int b_1(\boldsymbol{r}) \cdot \frac{\delta \mathbf{M}(\mathbf{r})}{\delta t} dV, \tag{3.14}$$

where $b_1(\mathbf{r})$ is the field per unit current generated at the spin packet by the coil. For systems that have separate transmit and receive coils, b_1 is replaced by a coil sensitivity function. Since the signal is proportional to the time derivative of the magnetization, which is proportional to B_0 and $\mathbf{M}$ is proportional to M_0, V_{coil} is proportional to B_0^2.

Many different types of RF excitation pulses are used in NMR and MRI. Here, we present just a few basic excitation pulse protocols to illustrate how nuclear spins can be excited. For MRI on human subjects, the applied RF fields are restricted to avoid substantial RF heating and ensure subject safety. The limit of RF exposure in MRI is set by a maximum specific absorption rate (SAR), typically 4 W/kg of whole body weight. The RF exposure limit can vary from country to country. SAR is determined by the electric fields induced by the RF coil, $\mathbf{E}_{\text{RF}}$, the local conductivity, σ, and density, ρ, $\text{SAR} = \sigma \mathbf{E}_{\text{RF}} \cdot \mathbf{E}_{\text{RF}}/2\rho$. The simplest excitation pulse is a short-duration rectangular RF pulse, shown in Fig. 3.2(a), which is used for broadband nonselective excitation and is referred to as hard pulse. There are limitations to this type of excitation pulse and, as seen in Fig. 3.3, it is difficult to excite spins uniformly. One method to overcome these limitations is to use composite pulses.[28] Figure 3.4(a) shows a Bloch simulator response to a simple rectangular 180° pulse, and Fig. 3.4(b) shows a composite pulse exciting the same spin ensemble with B_0 and B_1 inhomogeneities. The composite pulse consists of a 90° x-axis, a 180° y-axis and a 90° x-axis pulse. The

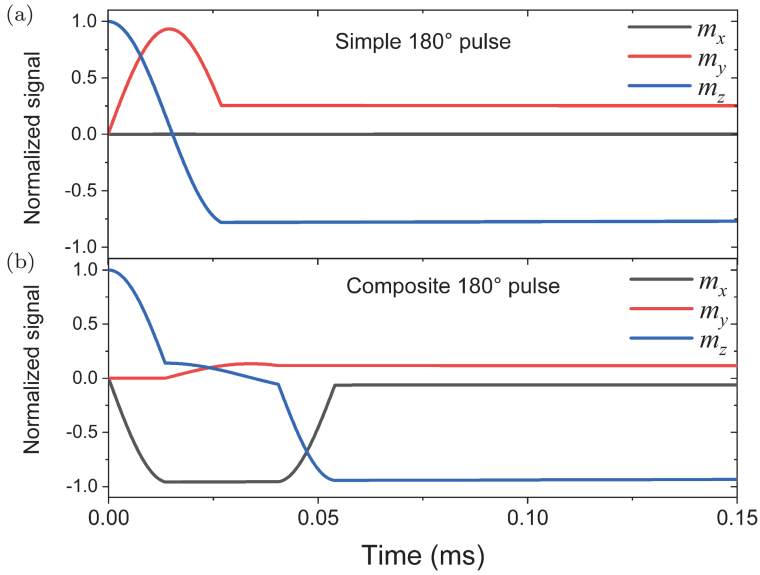

Fig. 3.4. (a) Response, calculated using a Bloch simulator, to a simple rectangular 180° pulse and (b) a composite 180° pulse for the same spin packet ensemble. The composite pulse is more efficient inverting all of the spins despite having a distribution of B_1 and ΔB_0.

180° y-axis pulse will advance spins whose flip angle was less than 90°, while retarding spins whose flip angle was greater than 90°. This allows spins to have the same flip angle, after the second 90° x-axis pulse, even though B_0 and B_1 vary. This is seen in Fig. 3.4, where the z-axis polarizations after the simple and composite 180° pulses are -0.778 and -0.974, respectively. The composite pulse is more efficient at inverting the spins ($m_z = -1$ would be maximum efficiency).

Shaped RF pulses, where the magnitude and phase of the RF envelope vary in time, are used for both frequency and spatial selection of excited spins. There are many different types of shaped pulses that can excite different chemical species and, through the use of magnetic gradients, excite them at different locations (see Fig. 3.9 as an example of simple slice selection RF pulse). Multiple frequencies can be combined for simultaneous multislice excitation. Although most excitation pulses use precise timing to control the precession of the magnetization around $\mathbf{B}_{\text{eff}}(t)$, there is another class of pulses, adiabatic pulses, that does not require precise control of timing. Adiabatic RF pulses are amplitude and phase-modulated pulses in which the moment is always kept close to the effective field $\mathbf{B}_{\text{eff}}$. Adiabatic refers to

the requirement that $\mathbf{B}_{\text{eff}}$ changes slowly, so that $\mathbf{M}$ may follow it. The spin excitation is relatively insensitive to pulse timing; however, the total pulse duration must be shorter than the relaxation times, and hence these pulses are also referred to as "fast passage."

3.1.5. *Simple pulse sequences*

There are many pulse sequences for NMR and MRI, and they can get very complex with many subtleties, all of which are important to gain an understanding of what the signal represents. A pulse sequence controls the output of amplitude and the phase of one or more RF channels, gradient channels, and input from one or more RF channels. Inputs can have 8–64 channels for typical head coils or a single input from a body coil. There may be other channels to synchronize with patient inputs or other complementary measurements. These include cardiac and respiratory gating, synchronizing with an acoustic transducer in magnetic resonance elastography or synchronizing with mental tasks or visual inputs in functional MRI studies. Here, we look at only the simplest pulse sequences to understand the challenges of getting quantitative information and to understand sources of error.

An important parameter in all pulse sequences is the repetition time TR, which is the length of time between corresponding consecutive points on a repeating series of pulses and detected signals. Given that spins have a long memory, typically seconds, the result of a pulse sequence will depend on the initial state of the magnetization, which in turn depends on its past history.

A spin echo sequence relies on the ability to rephase an ensemble of spins that have been dephased by precessing in a distribution of static fields. By applying a 180° pulse at a time TE/2 about x- or y-axes, the spins that have a phase advance become retarded, whereas the spins that have been retarded become advanced. At a time TE, the spins will again be in-phase, resulting in a signal referred to as a spin echo. A Bloch simulation of a spin echo sequence is shown in Fig. 3.5. The time between the excitation and the echo, TE, is referred to as the echo time and the 180° pulse as a refocusing pulse. A signal proportional to the amplitude of the FID will decay as $S(TE) = S_0 e^{-\frac{TE}{T_2}}$, whereas the linewidth of the FID is given by $\frac{1}{\pi T_2^*}$.

The Bloch simulations presented in this section are performed on a large number of spin packets with B_0, B_1 inhomogeneities, along with many other nonidealities found in real systems, such as timing jitter, transmit phase errors. The displayed signal includes coil sensitivity factors, electronic, and coil noise, and receive phase errors. The nonidealities, in this case, are chosen

to model a real NMR system that was used to take data in this section. The nonidealities and the modeling of measurement uncertainty for these data are discussed in NIST SP250-97.

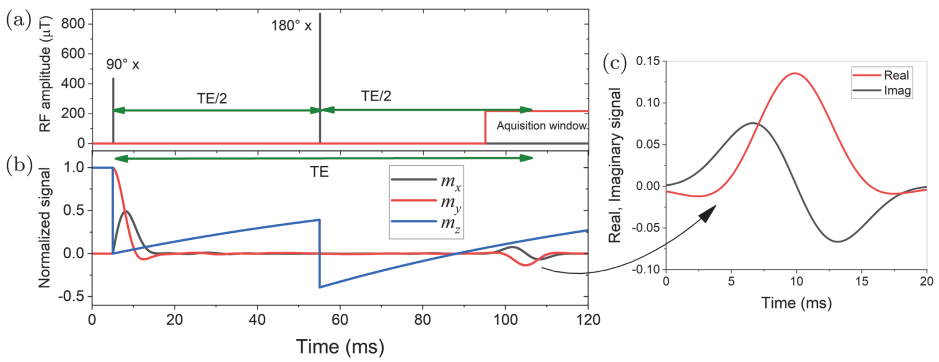

Fig. 3.5. Simple spin echo sequence that applies a 180° pulse at a time TE/2 on x- or y-axes, then records a spin echo at a spin echo time transverse electric (TE). (b) Calculated response of an ensemble of spin packets with $T_1 = 100\,\text{ms}$, $T_2 = 50\,\text{ms}$, and $T_2^* = 10\,\text{ms}$. An ensemble of 5000 spin packets was used in the calculation with a Gaussian B_0 distribution with a standard deviation of $1\,\mu\text{T}$. (c) A magnified plot of the spin-echo signal that is recorded.

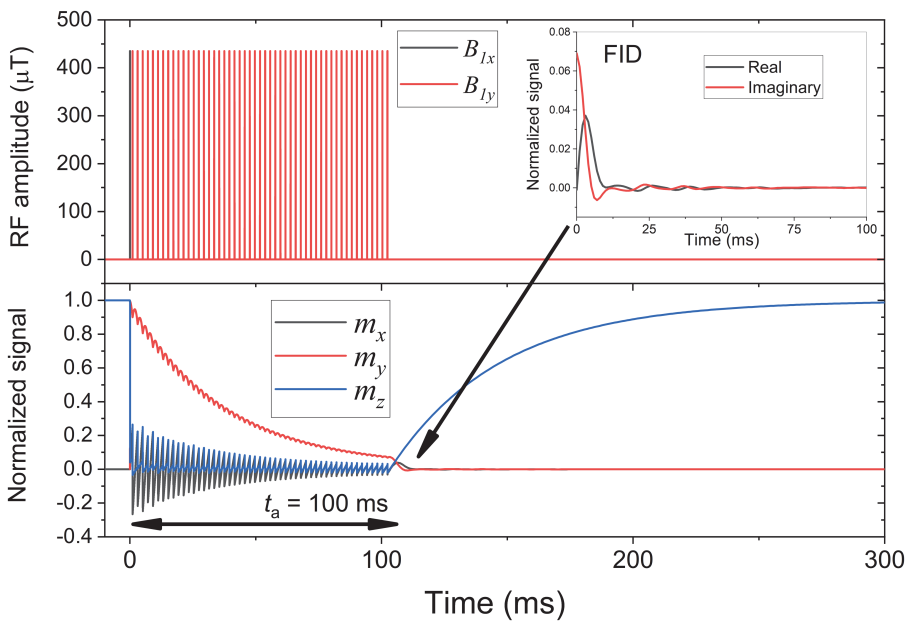

Fig. 3.6. Bloch simulation of a Carr–Purcell–Meiboom–Gill (CPMG) sequence with 50 refocusing pulses. The delay before and after the refocusing pulse is 1 ms.

Sequences with multiple refocusing pulses can be used. One such pulse sequence, the Carr–Purcell–Meiboom–Gill (CPMG) sequence[29] used to measure T_2, is shown in Fig. 3.6. Here, the spins are tipped into the transverse plane with a 90° x-axis pulse, then refocused with a series of 180° pulses on y. The FID is then recorded at a time $t_a = n(2\tau_{cp} + t_{180})$. Since the initial part of the magnetization decay is continually refocused, it decays with a time constant T_2. The measured FID at time t_a decays with time constant T_2^*.

Fitting the exponential decay of the signal, here defined as the integrated real part of the spectra, will give $S(t_a) = S_0 e^{-\frac{t_a}{T_2}}$. Sample NMR data from a CPMG sequence are shown in Fig. 3.7 along with an exponential fit to obtain $T_2 = 30.587$ ms. The inset shows the real part of the FID spectra, which are integrated to obtain the normalized signal. NMR measurements of T_2 can be accurate to better than 1% if the temperature is precisely controlled. For the MRI, standard CPMG sequences are problematic because they involve

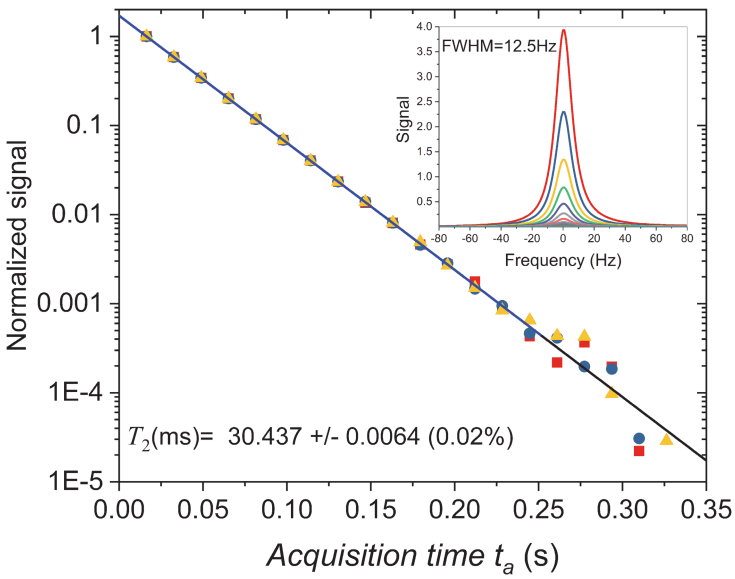

Fig. 3.7. Signal obtained by integrating the real part of the free induction decay (FID) spectrum (shown in the inset) versus acquisition time for a Carr–Purcell–Meiboom–Gill (CPMG) sequence for an MRI phantom calibration solution $NiCl_2$-12 at 20 C. The exponential fit to the data gives $T_2 = 30.437 \pm 0.006$ ms, which measures the intrinsic spin dephasing time. The full-width half-maximum (FWHM) linewidth of the spectrum gives a $T_2^* = 25.4$ ms, which measures the intrinsic plus extrinsic spin dephasing times. The recovery time, the time between the end of the pulse sequence to the beginning of the next, is always greater than 5 T_1.

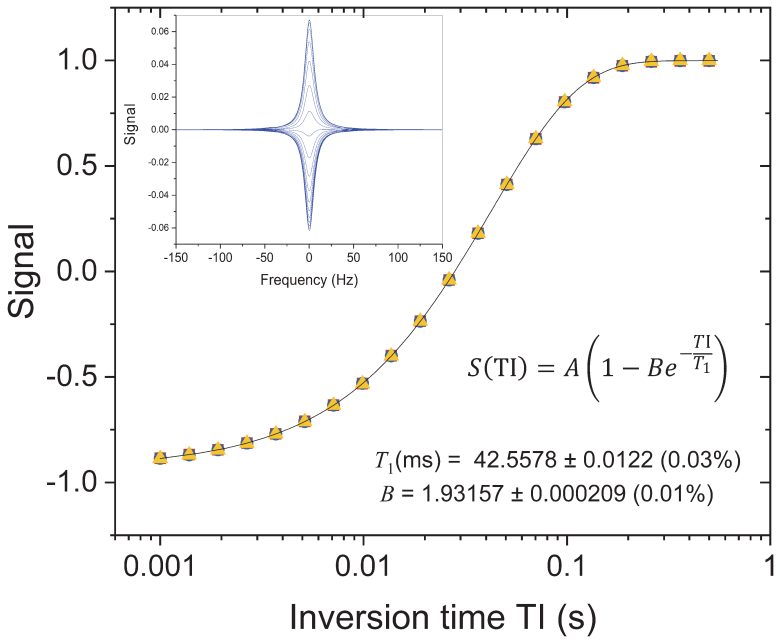

Fig. 3.8. Nuclear magnetic resonance (NMR) inversion recovery (IR) data for the MRI phantom calibration solution $NiCl_2$-12 at 20 C, with fit shown in black line. The measured T_1 is 42.558 ± 0.012 ms. The inset shows the real part of the Fourier transforms of the free induction decays (FIDs). The signal is the integral of the spectra.

a large number of 180° pulses, which may cause the RF dose to approach the SAR maximum.

Inversion recovery (IR) sequences invert the magnetization to lie opposite to the applied field. The recovery of the moment to the equilibrium can be monitored to measure T_1, or the recovery time can be used for magnetization preparation. The magnetization will go through zero at a time $\mathrm{TI} = T_1 \ln 2$. By picking this inversion time judicially, the signal from particular tissues can be nulled. Data from a simple IR sequence are shown in Fig. 3.8, along with a fit to a simple exponential recovery model whose equation is shown on the plot. The initial 180° pulse is a composite pulse meant to compensate for B_1 nonuniformity. The B-parameter, defined in the equation in Fig. 3.8, is determined by the fit to be 1.93. This value deviates from the ideal value of $B = 2$, indicating that the initial magnetization is smaller than the fully recovered magnetization, due to a distribution of flip angles. The measured value of B-parameter is consistent with the B_1 field inhomogeneity required to fit the nutation data in Fig. 3.3.

3.1.6. *Spatial encoding*

Two-dimensional Fourier encoding starts with a slice selection gradient pulse. One or more slices can be selected by applying gradients along a particular axis. A shaped RF pulse, such as a truncated sinc pulse $B_1 = A\frac{\sin(\omega_b(t-t_0))}{t-t_0}$, is used to excite spins in a slice where the spins are in resonance. For the case that the slice-select gradient G_s is applied along the z-axis and the flip angle is small $\sqrt{M_x^2 + M_y^2} \ll M_z \approx M_0$, then[3]

$$\frac{dM_{xy}}{dt} = -i\gamma G_s z M_{xy} + i\gamma B_1(t) M_0, \tag{3.15}$$

where M_{xy} is the complex transverse magnetization, and $B_1(t)$ is the time-dependent RF field. This equation can be solved for the initial condition $M_{xy}(t=0) = 0$:

$$M_{xy}(t,z) = i\gamma M_0 \int_0^t B_1(\tau) e^{i\gamma z \int_t^\tau G_s(u)du} d\tau. \tag{3.16}$$

For the case of the sinc pulse with a duration $T_p \gg \frac{1}{\omega_b}$, the transverse magnetization after the pulse is proportional to the Fourier transform of the sinc function

$$M_{xy}(T_p) = \begin{cases} \frac{i\pi\gamma A\, M_0}{\omega_p} e^{-\frac{i\gamma G_s T_p z}{2}} & \text{if } |\gamma G_s z| < \omega_b \\ 0 & \text{if } |\gamma G_s z| > \omega_b. \end{cases} \tag{3.17}$$

The excitation bandwidth is $2\omega_p$ and excited slice thickness is $\delta x = 2\omega_p/\gamma G_s$. There is an additional z-dependent phase $\phi = \frac{\gamma G_s T_p z}{2}$ after this excitation pulse, so the spins are not precessing coherently. This is remedied by applying a refocusing gradient after the RF pulse, as shown in Fig. 3.11. Figure 3.9 shows an applied truncated sinc pulse, and the calculated magnetization response after excitation and refocusing gradient. Many RF pulses used in clinical systems cannot be described by simple waveforms and are based on computer-based design processes using the Bloch equations, such as the Shinnar–Le Roux algorithm.[30] Computer-generated pulses provide more careful control of RF phase properties, allowing better control of the slice profile, energy deposition, and pulse duration.

To test slice excitation profiles, a slice thickness/profile test can be made using a set of wedges, as shown in Fig. 3.10. The slice thickness, t, can be measured by multiplying observed ramp distance s, $w_{1,2}$, by $\tan(10^\circ)$: $t_{sl} = 1/2(w_2 + w_1)x\tan(10^\circ)$. Averaging both ramp orientations corrects, in lowest order, for errors due to the misorientation of the image slice plane

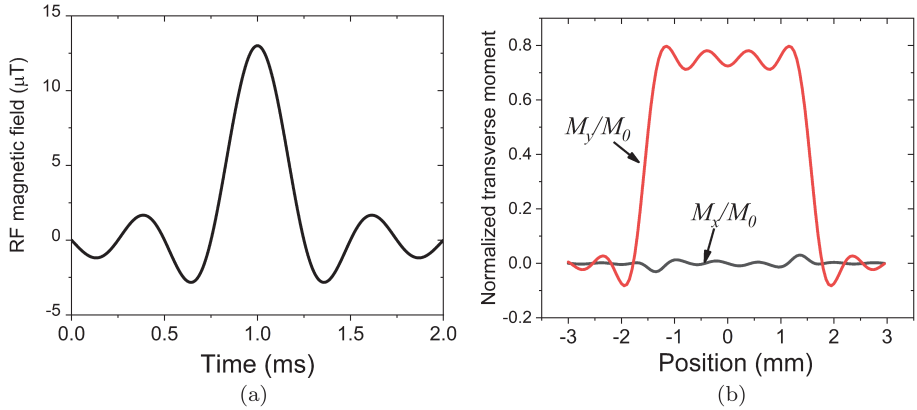

Fig. 3.9. (a) Truncated slice-select sinc pulse applied along the x-axis in the rotating reference frame. A 30 mT/m gradient pulse is applied concurrently. The excitation is designed for a 46° flip angle and 3-mm-thick slice. (b) Transverse components of the magnetization in the rotating frame as a function of position after the excitation and refocusing gradients.

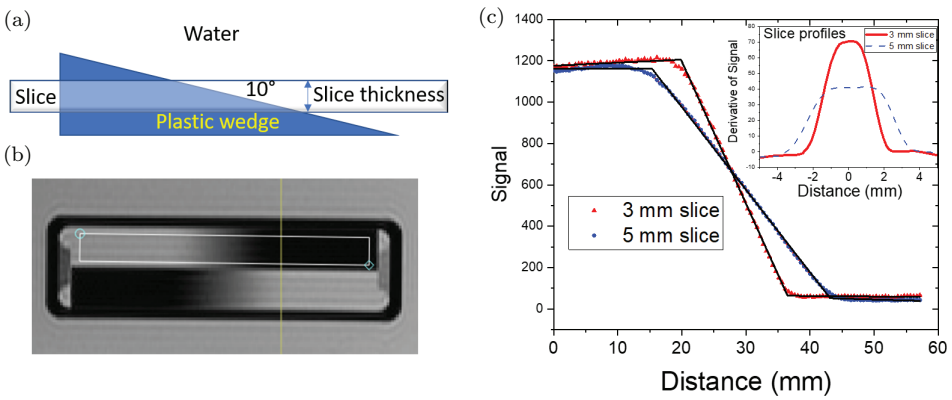

Fig. 3.10. (a) Schematic of 10° plastic wedge used to measure slice thickness and to assess slice profile. (b) Magnetic resonance imaging (MRI) of the pair of antialigned wedges. (c) Intensity scans across a wedge along with a fit to determine slice thickness. The prescribed slice thicknesses were 3.0 mm and 5.0 mm, whereas the measured slice thicknesses were 2.89 mm and 4.83 mm. The measured slice profiles are shown in the inset.

relative to the base of the wedges. The sharp transition from the linear to the constant regions indicates that, for this excitation pulse, the slice profile is nearly rectangular. This analysis follows guidelines found in NEMA MS 5-2010 standard document.[31]

After slice selection, the two-dimensional position of spin packets within a slice can be encoded using frequency encode and phase encode gradients. A frequency encode gradient, or readout gradient, is applied during the readout

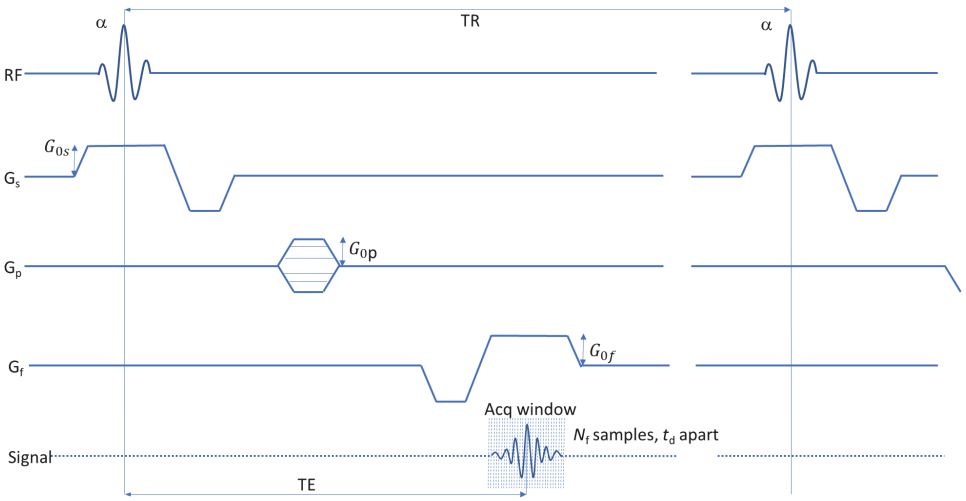

Fig. 3.11. Simple gradient echo pulse sequence with radio frequency (RF), slice, frequency encode, and phase encode output channels as a function of time. The bottom line shows the spin signal. G_s, G_p, and G_f are the slice, phase, and frequency encode gradients, respectively.

of the spin echo so that each spin packet precesses with a frequency that is proportional to the position along the frequency encode direction. A bipolar frequency encode gradient is shown in Fig. 3.11. The first negative lobe dephases the spins, whereas the positive lobe rephases them giving rise to a gradient echo. The state of the spin packet ensemble, in the presence of applied gradients, can be parameterized by a time-dependent k-vector, $\mathbf{k}(t) = \gamma \int_0^t \mathbf{G}_z(\tau) d\tau$. A phase encode gradient pulse of varying amplitude, as seen in Fig. 3.11, is used after the slice select pulse to provide well-defined phase advance along the direction perpendicular to the frequency encode gradient direction, within the selected slice. The signal at any given time is given by an integral over the spatial plane spanned by the frequency and phase encode gradient directions:

$$S(t) = \omega_0 b \delta x \iint M_{xy}(\mathbf{r}, t) e^{-i\boldsymbol{k}(t)\cdot\boldsymbol{r}} d^2\mathbf{r}. \tag{3.18}$$

Here, we assume that the coil sensitivity function, b, is constant and the transverse magnetization M_{xy} is averaged over the slice thickness δx. A finite set of samples N_f, usually 128, 256, or 512, are acquired within the acquisition window, giving one line of k-space. Two 90° phase-shifted signals, corresponding to real and imaginary parts of the signal, are acquired, from which the amplitude and phase can be calculated. The pulse sequence is repeated for N_p phase encode pulses until a full k-space image is acquired,

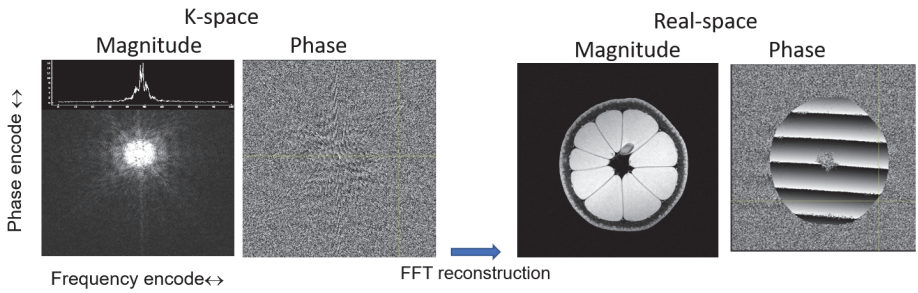

Fig. 3.12. k-space magnitude and phase data and reconstructed real-space magnitude and phase data for a lemon. The bands in the real-space phase data are due to 2π phase advances, which can be shimmed out. Where there is no signal, the phase is indeterminate and looks like white noise.

see Fig. 3.12. The receiver bandwidth of the signal is given by $r\text{BW} = 1/t_d$, where the dwell time t_d is the time between data acquisitions. The k-space image is converted to a real space image using a discrete fast Fourier transform, as seen in Fig. 3.12. The voxel spacings are given by $\Delta r_f = \frac{2\pi}{k_f} = \frac{2\pi}{\gamma G_f N_f t_d}$, $\Delta r_p = \frac{2\pi}{k_{fp}} = \frac{2\pi}{\gamma G_p N_p t_d}$ for frequency and phase encode directions, respectively. The fields of view are given by $N_f \Delta r_f$ and $N_p \Delta r_p$.

The two-dimensional data acquisition, with a rastered coverage of k-space, is commonly used; however, there are more complex acquisition schemes that use other k-space trajectories, such as spiral or radial acquisitions. Fourier encoding only represents one type of possible encoding of the spatial signal. As long as the obtained signal is a function of the image, one can potentially reconstruct the image. New reconstruction techniques using neural net systems can perform reconstruction of more general nonlinear encoding systems. With these artificial intelligence systems, there does not need to be an isomorphism between real-space and sensor-space images, since these systems can fill in missing information based on experience gained during training.[32]

3.2. MRI Transmit and Receive Systems

3.2.1. *MRI transmit and receive basics*

The vehicle for delivery of B_1 and readout of the precessing spins are RF coils. A single coil can function in both transmit (T_x) and receive (R_x) mode, or coils may be constructed for each function. The most common material for coil construction of MRI coils is either copper wire of varying widths or adhesive conducting copper tape. The signal-to-noise ratio (SNR) from a coil

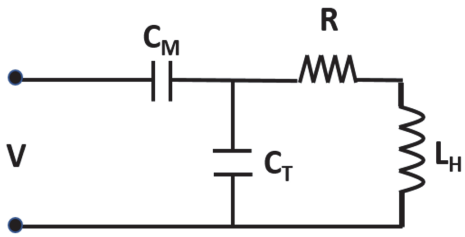

Fig. 3.13. A simple electrical schematic for many magnetic resonance imaging (MRI) coils. This schematic is for the majority of coils based on inductive coupling. In the ideal case, the resistance and inductance (L_H) arise only from the coil, and the parallel tuning capacitance (C_T) and series matching capacitance (C_M) are the only contributions to circuit capacitance. The material used to create the coil and connect it to the rest of the scanner represent additional sources of resistance and capacitance, which will affect the tuning of the coil. Proximity to other coils (i.e., gradient coils) can affect the actual inductance value.

is heavily dependent on the fill factor, or how much of the active space inside the coil is filled with the sample under study. For this reason, a variety of coil shapes and forms have been created for body part-specific imaging. The focus of this section is not the detailed history of coil design and construction in MRI. For an excellent comprehensive review of that topic, the reader is directed to Ref. 33. This section will identify a small but highly utilized sample of T_x/R_x coils used in the MRI experiment.

Any coil can be thought of as a resonant electrical circuit, the simplest schematic of which is given in Fig. 3.13. In the transmit mode, a voltage (V) produces a current (I_0), which in turn produces the magnetic field (B_1) that perturbs the spins from equilibrium. The coil efficiency, reported in magnetic field per square root power ($\mathrm{T/W^{-1/2}}$), determines how well current in the coil is converted to B_1. In the receive mode, the reverse process happens. The oscillating magnetic field generated by the spins returning to equilibrium induces a current in the coil, which produces a voltage that is then amplified, digitized, and postprocessed into the observed signal.

The operating frequency (in radians, $\omega = 2\pi f$) of the probe is determined by Eqs. (3.19) and (3.20), where C_T is the parallel capacitance, C_M is the series capacitance, L_H is the inductance of the coil, and R is coil resistance. The total capacitance (C_A) is the sum of C_T and C_M. For very low resistances, the ratio C_T/C_M is large and becomes smaller as resistance increases:

$$C_A = \left(\frac{1}{\omega}\right)^2 \frac{1}{L_H}, \tag{3.19}$$

$$C_M = \frac{RC_T}{2Z_0} + \sqrt{\frac{RL_H C_T^2}{Z_0(L_H - RC_T Z_0)} + \left(\frac{RC_T}{2Z_0}\right)^2}. \tag{3.20}$$

The impedance of the MRI system (Z_0) is 50 Ω and when the coil impedance is matched exactly to this value, it is said to be "critically coupled." Coil impedance of $Z_0 < 50\ \Omega$ or $Z_0 > 50\ \Omega$ represents "under-coupled" or "over-coupled" states, respectively. Coil coupling, and therefore efficiency, is impacted with each different sample type that loads the coil.

Any coil sufficiently large to interrogate a patient-sized sample is at the same time receiving a large amount of noise from the environment. The most common way around this in MRI is to use two separate coils for transmit and receive functions, for instance, a saddle or birdcage coil for the transmit function, and a small surface coil placed at the region of interest for the receive function.

3.2.2. *Simple saddle coil*

Saddle coils (Fig. 3.14), transverse-style resonators with magnetic field perpendicular to the main axis, have wide application but decreased sensitivity compared to solenoid-style resonators. The best RF homogeneity is generally achieved when θ, the angle between the two legs of the resonator, is 60°, but is also heavily dependent on the length of the resonator (similar to the simple solenoid). The provided B_1 can be increased by winding multiple loops on each side of the saddle coil. To reduce capacitive coupling between wires of each additional loop, a space of one wire diameter is left between the wires. Thus, the upper limit to this design is the size of the object to be imaged.

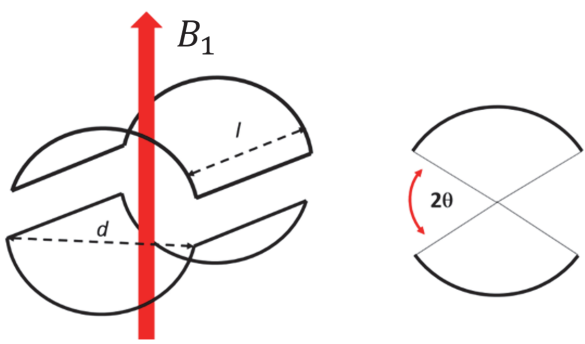

Fig. 3.14. Schematic of a simple saddle coil. The magnetic field created by a simple single-loop saddle coil is related to its dimensions (length, l and diameter, d) and the angle between the two legs of the resonator, θ. Most modern saddle coil designs make use of more than one loop on each side to improve the delivered B_1.

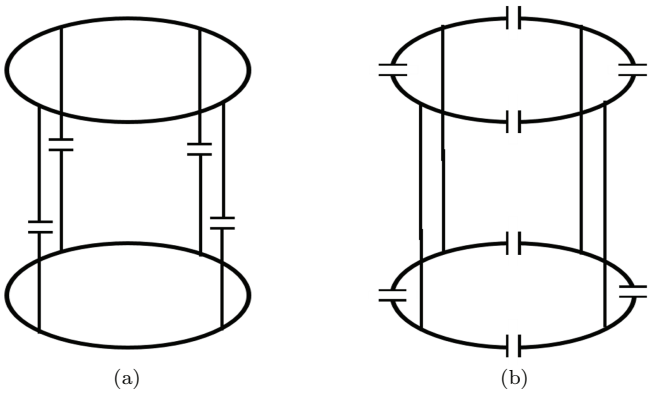

Fig. 3.15. Schematic of a four-leg birdcage coil. The low-pass (a) and high-pass (b) configurations are shown. The Hybrid configuration (not shown) is the combination of both low- and high-pass capacitor schemes.

3.2.3. *Simple birdcage coil*

The birdcage resonator was created in 1985 (see Ref. 34) to operate at higher frequencies than a saddle coil, while maintaining similar magnetic field homogeneity. A birdcage resonator shows various modes of resonance and can be turned into a double-resonance coil by tuning alternating legs tuned to different frequencies. Deviations in RF field homogeneity are more closely tied to design flaws. Resonator efficiency increases with the number of legs up to $n = 64$, with only a small increase in efficiency going to $n = 128$ legs.[33] One drawback of this resonator style is the high dependence of the B_1-field homogeneity on resonator symmetry, which is most assuredly broken upon introduction of a sample. Practical considerations of the effect of different capacitance values on the tuning of birdcage resonators are given in Ref. 35. Birdcage resonators can be constructed either as low-pass or high-pass versions depending on the configuration of capacitors used to tune the resonator (Fig. 3.15). Calculation of inductance is complicated by mutual inductance interactions between all legs and rings of the resonator. However, since 2002, open-source software[36] has been available to design all styles of birdcage resonator based on desired resonant frequency.

3.2.4. *Surface coil*

The simple single-loop surface coil provides an inhomogeneous magnetic field, but can provide high sensitivity (through high filling factor) when targeted to small sample volume or region. The performance of the surface coil is heavily dependent on proximity to the sample under study. However, the coil can be placed "too close," in which case the conducting properties of the

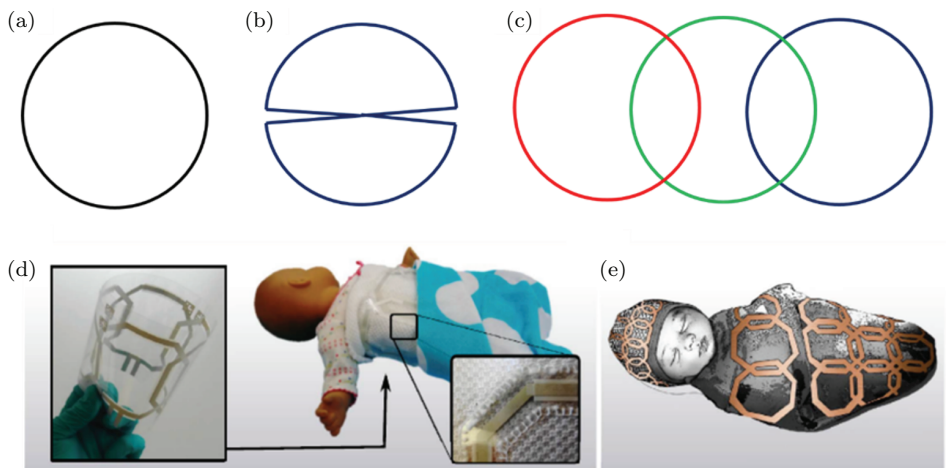

Fig. 3.16. Surface coils are highly versatile for magnetic resonance imaging (MRI) experiments. (a) The simplest surface coil is a single loop of copper, (b) but many other designs are employed such as the butterfly coil. (c) Multiple surface coils combined into a phased array (d) can be constructed to fit any body part. (d) and (e) Surface coils have been printed onto flexible polymer (polyethylene terephthalate) and incorporated into blankets, which can be used to image newborn patients (reproduced from Ref. 37).

sample (lossiness) can cause a decrease in efficiency. In addition, the signal from high magnetic flux regions can vary uncontrollably, which is deleterious for quadrature spectroscopy.

Surface coils are commonly employed in receive-only mode. The power in the application of surface coil(s) stems from imaginative higher-order combinations of the simple single-loop unit (Fig. 3.16). A series of overlapping surface coils, where each coil goes to a separate receiver, is called a phased array and commonly used in modern MRI. Surface coils can be wound in any noncircular shape to fit the sample, and even printed onto fabric. As one example of the utility of surface coils, screen-printed flexible MRI receive coils were recently created and installed within infant blankets.[37]

3.2.5. *Advanced high frequency methods: Traveling wave MRI*

Signal excitation in MRI must be uniform, so that readout changes are only dependent on the structure or pathology changes in the anatomical region of interest. The resonators described in the above sections are based on Faraday induction and the creation of standing RF waves within the resonator space for generation of the uniform magnetic field. At the common MRI field strength of 1.5 T, the free-space wavelength of the operating frequency

(64 MHz) is 4.7 m. The effective wavelength is decreased further (∼70 cm) due to the permittivity and conductivity of tissue[38] and is still larger than the bore size and target volume. At 3 and 7 T and higher, the effective wavelength quickly becomes smaller than the structure under study, producing a nonuniform RF field. The result of this nonuniform field at 3 T is signal degradation, and at 7 T a total signal loss.

An interesting workaround introduced in 2009 is traveling wave (TW) MRI.[39] TW-MRI takes advantage of a completely different method of generating EM radiation: The use of a waveguide that couples into specific modes of transverse electric (TE) or transverse magnetic (TM) fields. The circular waveguide is composed of the bore of the MRI magnet and a simple antenna excites the allowed modes in the bore. An important parameter for TW-MRI is the cutoff frequency (f_C), which determines the lowest frequency that will propagate into the bore/waveguide, and therefore be useful for MRI. The cutoff frequency is inversely proportional to the bore diameter — the wider the bore diameter, the lower the value of f_C.

Removal of close-coupling inductive resonators does lessen the effects of sample loading; however, TW-MRI is sensitive to reflections of radiowaves at the boundaries between regions with different wave impedances (i.e., tissue and air). In addition, TW-MRI is susceptible to sources of resistive noise (tissue) anywhere in the waveguide active volume, making it less sensitive for the receive operation. Combination of waveguide excitation with localized inductive coils for the receive operation may produce the best MRI experiment. Another use of locally placed passive inductive coils has shown improved B_1 delivery when used as part of a waveguide MRI experiment at 7 T.[40]

3.2.6. *Transmit/receive summary*

Understanding the MRI transmit/receive system is paramount in executing the quantitative MRI experiment. Substantial effort has been devoted to building and characterizing different coil types which (1) perform well from the electrical/instrument standpoint, (2) can be easily applied to human subjects, and (3) support image acquisition in the shortest time possible. Since these design criteria are essentially orthogonal to one another, a wide variety of different coil types have been invented for different MRI applications.

3.3. Accurately Measuring Physical Parameters with MRI: Phantoms

MRI has been traditionally used as a qualitative imaging technique with images interpreted by professional radiologists. We make a distinction

between images, where the voxel values have no intrinsic meaning, versus a map, in which voxel values are quantitative parameters with appropriate units. Images can be used to obtain quantitative biomarkers, such as tumor volume, cardiac volumes, and knee cartilage thickness. However, maps have a much larger information content, with each voxel being a quantitative parameter. There has been an increase in the use of MRI as a precision measurement system to create maps of key biomarkers related to cancer, neurological disease, coronary disease, musculoskeletal health, among others. These biomarkers have the potential to improve clinical diagnostics and are important in the development and efficacy determination of drug, radiation, and ablation therapies. *In vivo* measurements of biomarkers need to be validated using SI-traceable imaging calibration structures referred to as phantoms.

Figure 3.17 shows a system phantom developed by the National Institute of Standards and Technology (NIST) and International Society of Magnetic Resonance in Medicine (ISMRM),[41] which has been commercialized. This phantom contains three contrast arrays, a $NiCl_2$ and a $MnCl_2$ array for T_1, T_2, and a proton density (PD) array. It also contains a resolution inset, a fiducial array for characterizing geometric distortion and B_1 inhomogeneity, and a set of ramps for determining the slice profile. The $NiCl_2$ and a $MnCl_2$ arrays for T_1 and T_2 measurement, will be discussed in the relaxometry

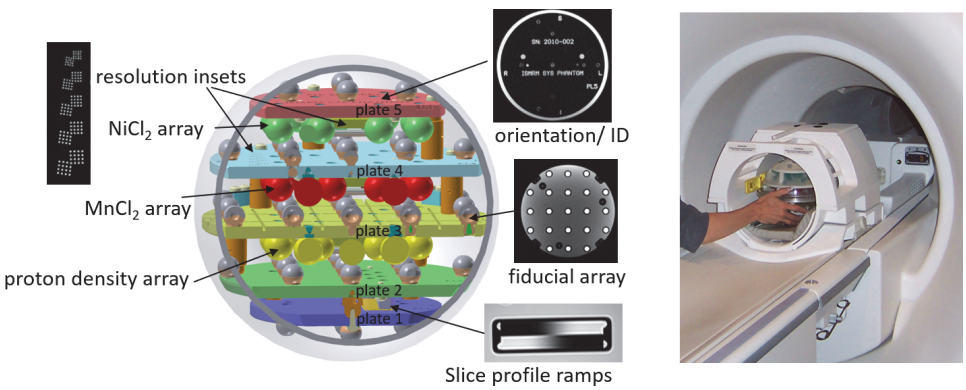

Fig. 3.17. The National Institute of Standards and Technology (NIST)/International Society of Magnetic Resonance in Medicine (ISMRM) system phantom is a 200-mm diameter water-filled sphere with multiple components for testing scanners, scanner stability, interscanner comparability, and accuracy of quantitative imaging protocols. The left image shows the design of the phantom indicating fiducial array, $NiCl_2$ and $MnCl_2$ arrays for T_1 and T_2 measurement, proton density array as well as the resolution and slice profile insets. The system phantom being loaded into a head coil for scanning is shown in the right panel.

section. Here, we will briefly discuss PD, resolution, geometric distortion, and slice profile.

3.3.1. *Proton density*

PD is measured using a short TE (to minimize signal loss from T_2 relaxation), and a long TR (to ensure complete repolarization of the spins to minimize T_1 dependence). An image of the PD array, which contains D_2O/H_2O solutions with differing proton concentrations, is shown in Fig. 3.18. There are 14 spheres with PD ranging from 5% to 100% (PD = 5% is 5% H_2O, whereas PD = 100% is pure H_2O). Circular region-of-interests (ROIs) with 10.0-mm diameters are drawn within the 16-mm internal-diameter spheres. The average signal within the ROI is plotted versus PD. The signal increases linearly for small TE. As TE increases, T_2 relaxation becomes more important, and the signal is no longer proportional to PD. Gibbs ringing artifacts, due to the Fourier transform of sharp contrast features, can be seen (lower right inset in Fig. 3.18) around the low-signal polypropylene sphere walls. There is nonuniformity of the voxels within the uniformly filled sphere, not

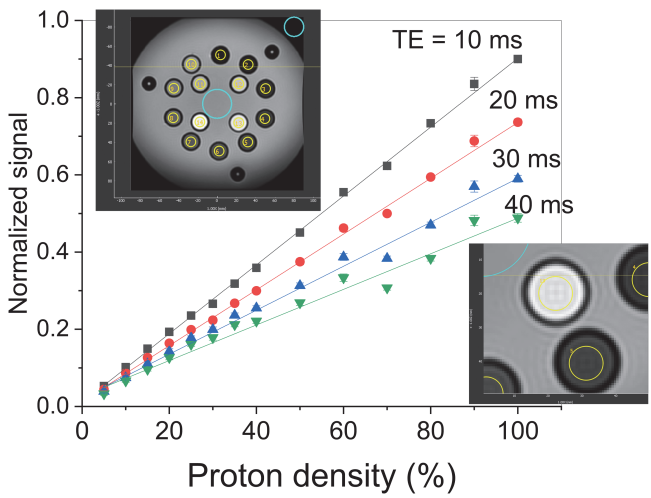

Fig. 3.18. Proton density (PD) array. The upper-left inset shows a gradient echo image (3 T, TR 3000 ms, 0.70 mm pixel size, slice width = 6 mm) of the PD array with 14 region-of-interests (ROIs). Plot of intensity versus PD for different echo times (TE = 10, 20, 30, 40 ms). Error bars give the standard deviation of the 177 voxels within the ROIs. The lower-right inset shows nonuniformity of PD = 90% sphere and Gibbs ringing artifacts. The center and exterior ROIs in blue are for signal-to-noise analysis done on a pair of identical images (Courtesy of the Brain Imaging Center University of Colorado Health Science Center).

consistent with Gaussian noise. All of these nonidealities must be accounted for to understand the accuracy of quantitative image-based measurements.

3.3.2. *Geometric distortion*

The system phantom contains a fiducial array of fifty-seven 10.0-mm internal-diameter spheres spaced on a 40.0-mm grid (see Fig. 3.19). By comparing the apparent position of the spheres with the actual positions, a geometric distortion map can be obtained.[42] System-dependent image distortion can be due to nonlinear gradients, static field inhomogeneities, induced eddy-current-generated magnetic fields, and can often be corrected for with software. There are trade-offs between designing linear gradients and the desire to have high magnitude gradients, as well as large open-environment bore geometries. Figure 3.20 shows the system phantom with distortion clearly seen in Fig. 3.20(a) along the anterior/posterior (A/P)

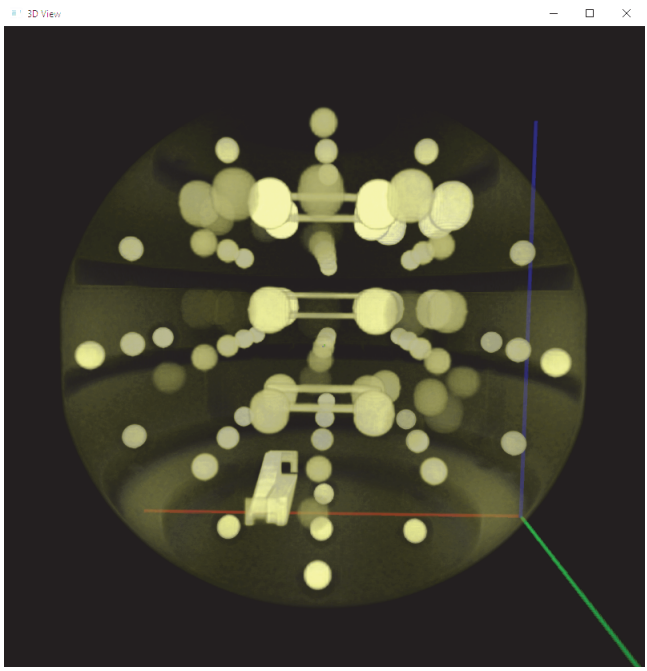

Fig. 3.19. Projection of three-dimensional gradient echo multislice image of the National Institute of Standards and Technology (NIST)/International Society of Magnetic Resonance in Medicine (ISMRM) system phantom. The voxel size is 0.98 mm isotropic, field of view is 250 mm, TR = 5.9 ms, and TE = 1.37 ms. The small spheres form a precise array on a 40.0 mm grid to allow geometric distortion analysis. The larger spheres are the contrast arrays. Also seen are slice profile ramps and rectangular resolution insets.

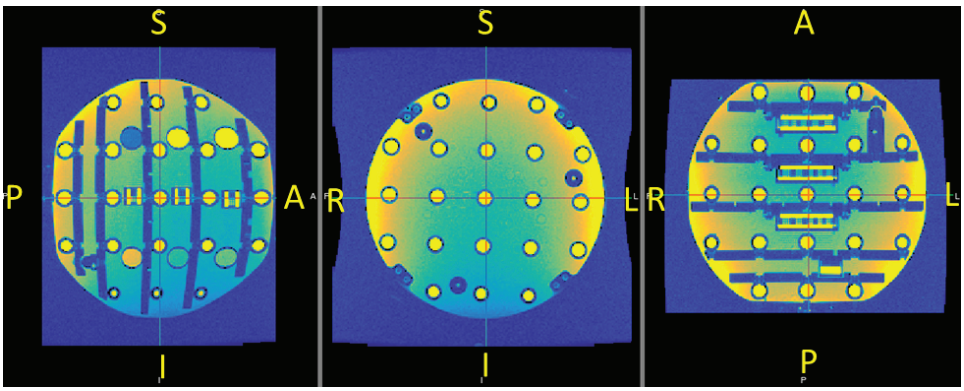

(a) (b) (c)

Fig. 3.20. Images of the National Institute of Standards and Technology (NIST)/ International Society of Magnetic Resonance in Medicine (ISMRM) system phantom. (a) Sagittal image without gradient distortion corrections showing distortion in the anterior/posterior (A/P) direction. (b) Coronal image with distortion correction in the left/right (L/R) and superior/inferior (S/I) directions (note the image outline shows the magnitude of the distortion corrections). (c) Axial slice with distortion corrections (Images courtesy of Dr. Jeffrey L. Gunter. Mayo Clinic).

direction. Figures 3.20(b) and 3.20(c) show the system phantom with distortion corrections in the coronal and axial planes. In general, three-dimensional distortion corrections are required and depend on how the image is centered relative to the magnet isocenter.

The nonlinear gradient distortion, static field inhomogeneities, and eddy-current-induced magnetic fields are system-dependent effects that can cause geometric distortion in an image. These distortion effects can be understood and corrected through phantom studies. There are other patient-dependent distortions due to magnetic susceptibility and chemical shifts. Correcting patient-dependent geometric distortions is becoming more critical for image-guided therapies such as MRI-guided radiation therapy.

A more complex example of geometric distortion in breast imaging is shown in Fig. 3.21, which shows the NIST/University of California San Francisco breast phantom and geometric distortion data.[43] In addition to tissue mimics, T_1, and diffusion arrays, this phantom contains a geometric distortion inset consisting of an array of uniform holes filled with water. Here, a systematic left/right geometric distortion was observed for a particular set of pulse sequences meant to map water diffusion.[44] The pulse sequence, single-shot echoplanar imaging (SS-EPI) is used to map the apparent diffusion coefficient of water to better delineate and evaluate breast lesions and

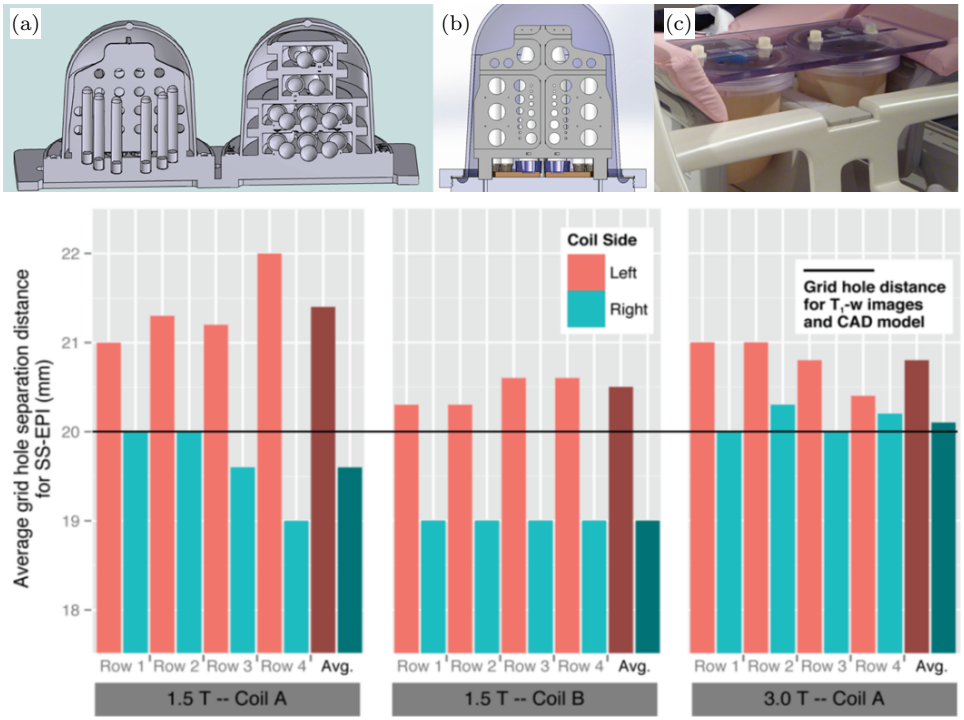

Fig. 3.21. Geometric distortion data taken on two different coils on two different scanners showing a distinct left–right asymmetry for the single-shot echoplanar imaging (SS-EPI) sequence used to obtain water diffusion maps.[44] The grid hole separation (as prescribed in the computer-aided design [CAD] model) is 20 mm and is shown by the black line.

tumors. Usually, geometric distortions are symmetric about magnet isocenter. In this case, they are asymmetric and are related to the direction in which k-space is sampled.

3.3.3. *Resolution*

An image $I(\mathbf{r})$ is a representation of an object $O(\mathbf{r})$ and maps some properties of that object at a location $\mathbf{r}$ into voxel values. Due to the finite resolution of all imaging systems, a point in the object will be mapped into a region in the image described by a point spread function (PSF)[3]:

$$I(\mathbf{r}') = \int O(\mathbf{r})\mathrm{PSF}(\mathbf{r} - \mathbf{r}')\mathrm{d}\mathbf{r}. \tag{3.21}$$

An important component of the PSF in MRI is due to finite sampling. Assuming that the image is in the x,y plane with fields of view given by

L_x, L_y, and number of samples N_x and N_y, this component is given by

$$\mathrm{PSF}(x,y) = \frac{e^{-\frac{i\pi x}{L_x}} \sin\left(\frac{\pi N_x x}{L_x}\right)}{N_x \sin\left(\frac{\pi x}{L_x}\right)} \frac{e^{-\frac{i\pi y}{L_x}} \sin\left(\frac{\pi N_y y}{L_x}\right)}{N_y \sin\left(\frac{\pi y}{L_y}\right)}. \tag{3.22}$$

Defining the resolution as the effective width of PSF[3]:

$$\delta x = \frac{1}{\mathrm{PSF}(0)} \int_{-\frac{L}{2}}^{\frac{L}{2}} \mathrm{PSF}(x)dx. \tag{3.23}$$

The resolution due to finite sampling is $\delta x = \frac{L_x}{N_x}$ or the pixel width. This contribution to the resolution is often the dominant one, since obtaining highly sampled images, below the system resolution, creates excessive data processing and storage issues.

Figure 3.22 shows images of the NIST/ISMRM system phantom resolution inset along with line scans. The resolution inset is based on the one developed for the American College of Radiology (ACR) MRI phantom.[45,46] The resolution inset consists of 4×4 arrays of 16 fluid-filled holes with diameters ranging from 0.4 to 0.8 mm. Identical, but 10° rotated arrays, are also included to help assess the resolution differences when taken along special (e.g., frequency encode/phase encode directions) versus general directions. Using ACR guidelines for manually obtaining the resolution from these images, the resolutions are 0.5 mm horizontal and 0.6 mm vertical. This is close to the pixel size of 0.49 mm in both directions. Another, more quantitative method to evaluate the resolution is to determine from the line scans the array in which the modulation transfer function[f] and has fallen to 0.5, which also occurs between 0.6 and 0.5 mm. Also shown in Fig. 3.22 are the images with $4\times$ interpolation, which is usually preferred for human interpretation. However, there is no difference in the image resolution between (a) and (b), as seen in the line scans, which are similar. The image resolution is a strong function of the imaging protocol and parameters, including N_x and N_y and slice thickness.

3.4. Relaxometry

There is a large literature on nuclear spin relaxation with many recent comprehensive reviews.[8,47] There are many different methods to measure T_1,[48]

[f]The modulation transfer function is the magnitude response of an imaging system to sinusoids of different spatial frequencies. Here, the hole array approximates standard optical grating systems. MRI resolution standards with more conventional resolution insets have been proposed, although the ACR version was chosen because it is very compact and easily interpreted by humans.

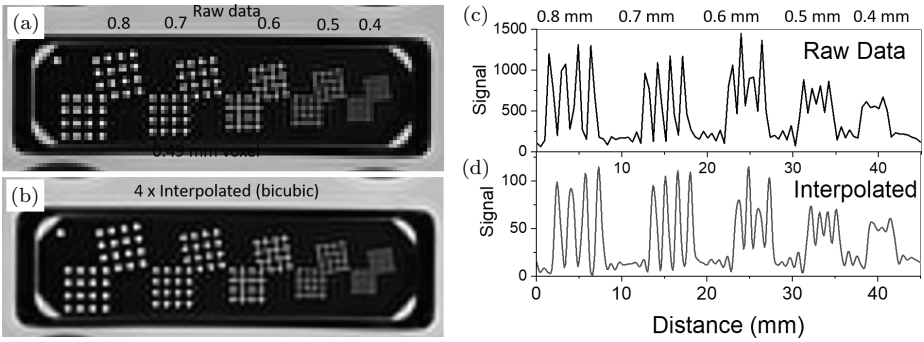

Fig. 3.22. Resolution inset in National Institute of Standards and Technology (NIST)/International Society of Magnetic Resonance in Medicine (ISMRM) system phantom styled after the American College of Radiology (ACR) resolution inset. (a) Shows the raw data, whereas (b) shows interpolated data where the number of voxels is expanded by a factor of 4 in each direction. A two-dimensional spin echo sequence was used with $L_x = 250\,\text{mm}$, $L_y = 250\,\text{mm}$, $N_x = 512$, $N_y = 512$, TR $= 5000\,\text{ms}$, TE $= 63\,\text{ms}$, slice thickness $= 4.0\,\text{mm}$, bandwidth $= 225\,\text{kHz}$. (c) and (d) Show intensity scans through the nonrotated hole arrays for the raw and 4× interpolated data, respectively.

and new methods are being published each year. Many of the proposed T_1-measurement methods are focused on faster, lower power techniques that are pragmatic for use in MRI on human patients. Similarly, there is extensive literature on measuring T_2, as well as analysis of sources of error in these measurements.[49] The hope is, given sufficient quantitative parameters, better analysis and clinical decisions can be obtained. For example, it may be possible to automatically segment white matter, gray matter, and brain lesions based on quantitative maps of T_1, T_2, and other parameters. This goal remains challenging due to the wide dispersion of measured values and the inability to distinguish the component due to variability in the tissue versus variability in the measurement technique. A recent review states:[8] "The hope that each individual tissue would have particular range of normal T_1 and T_2 relaxation times and that reliable measurement of these times would enable an unambiguous identification of different tissues seems to fade with the large spread of T_1 and T_2 relaxation times found in the literature. This spread of values indicates that there is not a common set of reference values for the relaxation times of tissues, and that there is a huge amount of ambiguity surrounding the measurements." Here, we look at some primary measurement methods for T_1 and T_2 that are used to validate other techniques, which are appropriate for clinical applications requiring fast, low-RF-power acquisitions and look at how standard phantoms can be used to understand

measurement uncertainties. The data presented is from the NIST/ISMRM system phantom, which contains two arrays with paramagnetic ions in water to modulate T_1 and T_2 over a wide range of values. One array is doped with $NiCl_2$, the other with $MnCl_2$. The $NiCl_2$ array has the advantage that its properties are more stable with temperature and magnetic field, whereas the $MnCl_2$ array has T_1 and T_2 values that are closer to human tissue.

3.4.1. T_1 *measurement*

A gold standard for T_1 mapping is the IR pulse sequences described in the section on simple pulse sequences. Most MRI systems predominantly use magnitude information and do not save phase data. The phase component of MRI datasets can be hard to obtain without artifacts in contrast to the NMR data previously shown. A T1-IR dataset, from a 3-T scanner using a head coil with TR = 4500 ms, is shown in Fig. 3.23. Circular ROIs, with 10 mm diameter, are drawn in the different T_1 spheres. The average signal for each

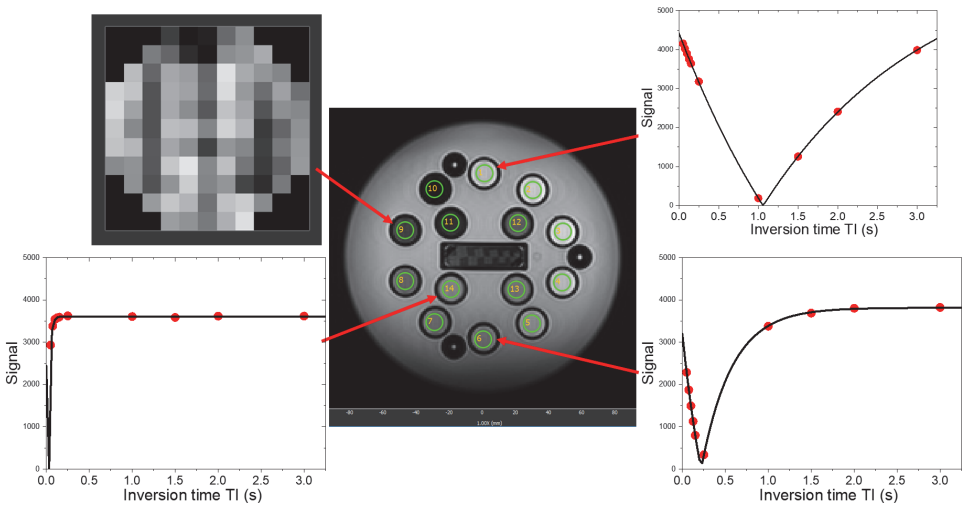

Fig. 3.23. Image of T_1 array in National Institute of Standards and Technology (NIST)/International Society of Magnetic Resonance in Medicine (ISMRM) system phantom, taken on a 3 T scanner with TR = 4500 ms, showing 14 regions of interest (ROIs) with T_1 values ranging from 20 to 2000 ms. The data consist of an image stack with 10 *TI* values ranging from 50 to 3000 ms. The upper left plot shows a zoom-in of ROI 9 to show the voxels and noise in the ROI. The average signal divided by the standard deviation of the signal within an ROI is approximately 40. The surrounding plots show the average signal in a given ROI plotted as a function of TI with fits to the model described in the text, which yields T_1 and the asymmetry parameter, B. We thank Wisconsin Institutes for Medical Research for providing the scans.

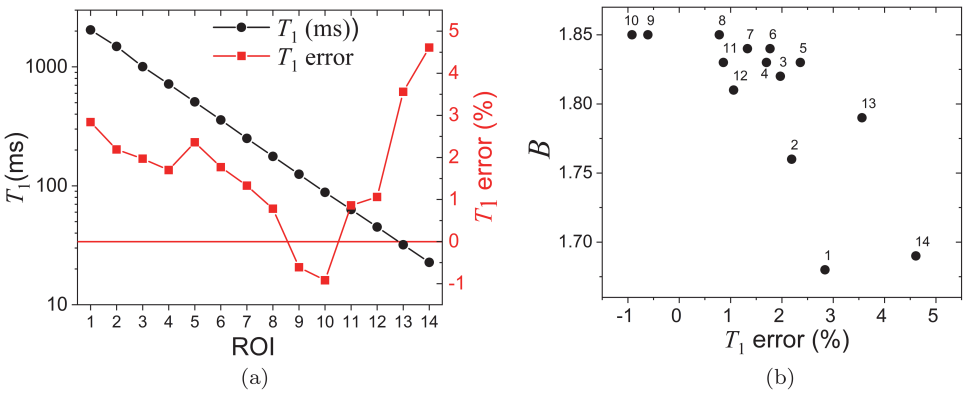

Fig. 3.24. (a) Plot showing T_1 values from fits to the Inversion recovery (IR) model. The red plot shows errors relative to more accurate nuclear magnetic resonance (NMR) measurements. (b) Plot of the asymmetry parameter, B, versus the T_1 error. Labels indicate ROI number; ROI number and T_1 are inversely proportional.

ROI for each TI is fit with a function of the form $S(\mathrm{TI}) = |A(1 - Be^{-\frac{\mathrm{TI}}{T_1}})|$ to yield T_1, as shown in Fig. 3.23. This formula is correct when TR is much longer than T_1, which is a good approximation except for the longest T_1 spheres. Also shown is the error relative to more precise NMR measurements on the same solutions. Figure 3.24 shows the results of the fits, with T_1 values for all of the ROIs. The T_1 values were chosen to be logarithmically distributed to give a straight line on a semilog plot. The deviation of the MRI-measured values from more accurate NMR measurements is also shown. Errors are larger for the longest and shortest T_1 values. The B-parameter is plotted as a function of T_1 error, showing there is a correlation with B-values that significantly deviate from the ideal value of 2.0.

Another important source of uncertainty in the relaxation measurements of phantoms comes from imprecise control or measurement of temperature. For the solutions used in the T1-IR data below, the temperature variation is approximately 1.3%/°C. The observed bias may be due to a discrepancy between the phantom temperature and the NMR reference data, which was taken at 20°C.

Another pulse sequence protocol used to measure T_1 is a variable flip angle (VFA) sequence. The flip angle is varied and TR is short (<10 ms), so that the spins do not have time to relax back to equilibrium between excitations. At low flip angles, as seen in Fig. 3.25(a), the signal increases linearly as expected. Since the spins do not have time to fully relax when there is a large flip angle, the signal decreases. This is in contrast with the nutation data in Fig. 3.3, where the spins are always allowed to fully relax.

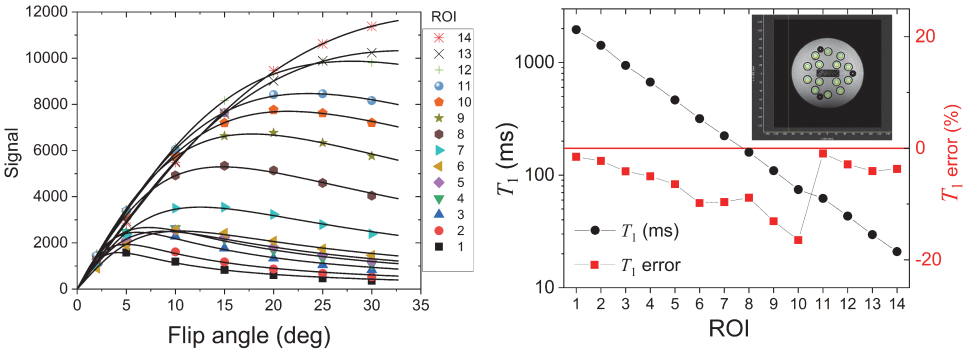

Fig. 3.25. (a) Signal versus flip angle for 14 $NiCl_2$ spheres in the National Institute of Standards and Technology (NIST)/International Society of Magnetic Resonance in Medicine (ISMRM) system phantom using a TR = 5.368 ms on a 3 T scanner. The scan time was 2 min 20 s. Solid lines are the fit to the model. (b) T_1 values extracted from fits along with error relative to nuclear magnetic resonance (NMR) measurements. We thank Wisconsin Institutes for Medical Research for providing the scans.

The model used to fit the data was

$$S(\alpha) = S_{90} \sin(\alpha) \frac{1 - e^{-\frac{TR}{T_1}}}{1 - e^{-\frac{TR}{T_1}} \cos(\alpha)}. \tag{3.24}$$

The error for the VFA data, Fig. 3.25(b), is significantly larger than for the IR protocol, Fig. 3.24(a). Additionally, correlations in the error with decreasing T_1 can be observed along with a radial dependence: The central four spheres (11, 12, 13, and 14) have the smallest errors. The scan time for the VFA sequence, however, is faster, with 120 images collected in 2 min 20 s, compared to the IR sequence that typically collects 10 images in 4 min.

3.4.2. T_2 *measurement*

Accurate T_2 measurements remain challenging for MRI because T_2 measurements are affected to a higher degree by imperfections in the RF pulses used during the experiment. The effect of imperfect RF pulses has been known and studied in the laboratory since the first clinical scanners were put into use in the mid-1980s. The problem was first highlighted in a series of papers by Majumdar in 1986–1987.[50,51] Application of an imperfect pulse results in incomplete tipping of the magnetization vector. The result is one longitudinal component and two transverse components. One of the transverse components experiences a phase reversal due to the RF pulse and one is not affected at all.[50,51] The transverse component, which is not sensitive to

phase, causes image "ghosting," and the longitudinal component contaminates the image with every successive pulse.[50]

An extensive body of research has grown around solving the effect of imperfect RF pulses, which specifically plague T_2. Efforts have been broadly focused on improving the geometric fidelity (i.e., removing distortions),[52–55] or use of phase cycling[56–59] or advanced correction methods[60–66] to remove the effect of unwanted stimulated echoes. Other efforts have also focused on hardware/method-derived errors such as coil cross talk,[67] or use of hard versus soft pulses in a CPMG imaging sequence.[68] These efforts have been developed in parallel with improvements of MRI in the clinic — making improvements in RF coils, gradients, pulse sequences, and imaging speed. These improvements often compensate for imperfect RF pulses instead of addressing the base problem of imperfect RF pulses first.[69] Quantitative T_2 analysis from MRI will require that both laboratory and clinical development paths recombine and integrate advances made in each arena.

Gold-standard NMR pulse sequences are too time-consuming for MRI, and slice selection introduces additional nonidealities, as detailed above. Figure 3.26 shows a T_2 map of the NIST/ISMRM phantom T_2 array produced by a clinical scanner. One can observe imperfections in the apparent T_2 in the uniform background, most likely due to B_1 inhomogeneities from the coil set. Disagreements between measurements of 40% or more are often seen, which can be greater than the differences in the tissues that need to be discriminated.

A common method to measure T_2 in MRI is a spin echo sequence. There are many different forms of spin echo sequences including fast spin echo and multi-spin echo sequences.[1] Here, we will only discuss the simplest spin echo sequences. Typical data, signal versus echo time, are shown in Fig. 3.27. Unlike the CPMG sequence used in Fig. 3.6, these sequences use widely spaced echoes that refocus on the same phase as used for the 90° phase excitation. These sequences can have large longitudinal moments when the refocusing pulses occur, which give rise to stimulated echoes when the RF fields are not uniform. Furthermore, B_1 inhomogeneities during slice selection for the 180° refocusing pulses contribute to additional errors. Some of these problems can be seen in Fig. 3.27, which include an anomalously low signal for the first echo, having alternating amplitude variations for even and odd echoes. Figure 3.28(a) shows data that have been fit with an exponential model after throwing out the first echo and points below the noise floor. The results are shown in Fig. 3.28(b) along with the error with respect to more precise NMR measurements. The problems using spin echo sequences for quantitative T_2 measurements have been extensively documented,[50,51,57]

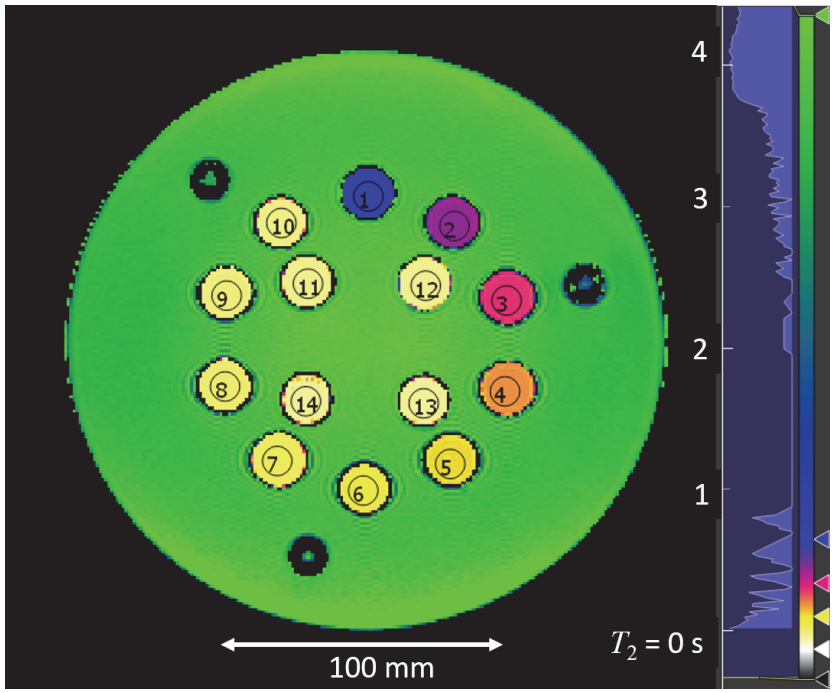

Fig. 3.26. T_2 map from a 3 T scanner using a spin echo sequence. Also shown, are region-of-interests (ROIs) used to determine T_2 values for the different solutions.

and more accurate mapping sequences have been proposed. These include broadening the refocusing pulse[65] with trade-offs of limiting the number and distance of the slices that can be obtained, or using adiabatic pulses[61,70] that require longer pulses with higher SAR available. New machine learning techniques, such as MR fingerprinting,[71] can fit many parameters simultaneously, including B_1 nonuniformity. These techniques, by using complex physics models, may be able to determine system nonuniformity as part of the fitting process. Finally, the lack of precise temperature control in clinical scanners and imperfect temperature agreement with the reference measurements may account for several percent error in phantom measurements. The lack of precise temperature control may be a confounding factor when determining the accuracy of T_2 measurement protocols.

In summary, although T_2 measurements in MRI have historically been difficult, much documented effort exists on how the problem may be overcome. In addition, novel methods, such as MR fingerprinting, offer a new path around the problem entirely. Current work in both laboratory and clinical arenas, coupled with strong reference objects such as the NIST/ISMRM

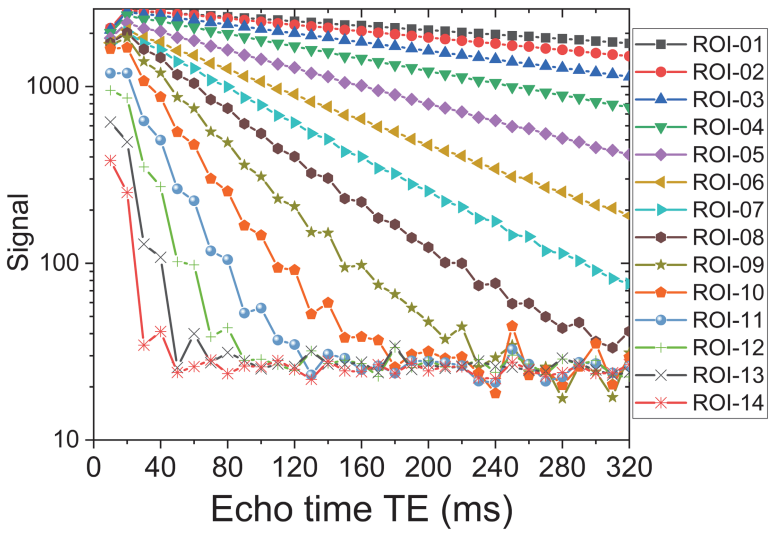

Fig. 3.27. Signal versus echo time for 14 ROIs in the National Institute of Standards and Technology (NIST)/International Society of Magnetic Resonance in Medicine (ISMRM) system phantom using a spin echo sequence on a 3 T scanner with TR = 5.0 s. Nonideal behavior can be seen in the anomalously low signal in the first echo and the oscillation of signal amplitude between even and odd echoes. Additional problems come from a poorly defined noise floor that can vary with ROI. We thank the North Shore University Health System for providing the scan data.

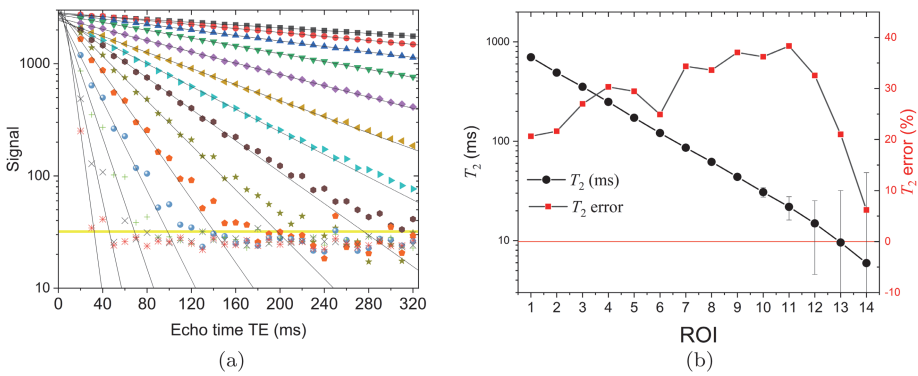

Fig. 3.28. (a) Spin echo data from Fig. 3.27 fit with a simple exponential model, where the first echo has been thrown out along with all data below the yellow line, which is near the noise floor. (b) Extracted T_2 values for the 14 regions of interest (ROIs) in the T_2 array of the National Institute of Standards and Technology (NIST)/International Society of Magnetic Resonance in Medicine (ISMRM) system phantom along with deviation from nuclear magnetic resonance (NMR) measurements made at 20°C.

phantom, should lead to improved quantitative T_2 measurements and provide the required accuracy for T_2 to become a reliable biomarker.

3.5. B_0 Distortion and Magnetic Susceptibility

B_0 distortions (magnetic field distortions along the z-axis) may be caused by nonuniformity of the applied field or by field distortions due to the varying magnetic susceptibility of the sample, patient, or patient implants. In many cases, these distortions are undesirable and give rise to imaging artifacts. Alternatively, B_0 distortions can provide important information about the type and health of various tissues. B_0 distortions are best seen in phase images using simple gradient echo sequences. The change in spin packet phase due to a local field variation δB_L is given by $\phi = \gamma_p \cdot \delta B_L \cdot \mathrm{TE}$, where TE is the echo time, the length of time that the spin ensemble evolves after uniform excitation. Figure 3.29 shows the MRI magnitude and phase images of a water-filled phantom with a vial of 5.0-mM $GdCl_3$ solution, which has an additional paramagnetic magnetic susceptibility component due to the spin $7/2\,Gd^{+3}$ ions. The lines observed in the phase image, in Fig. 3.29(a), are 2π phase jumps, indicating there is a residual field nonuniformity in the scanner, predominantly in the vertical direction, due to an imperfect shim. The distortions of the phase fronts around the vial containing the paramagnetic solutions are due to fields produced by the sample. When the phase is unwrapped and the linear background is subtracted (third frame in Fig. 3.29(a)), one can clearly see the contrast due to differences in magnetic susceptibility.

The local magnetic field differs from the macroscopic field and is given by the macroscopic field minus the Lorentz field. The Lorentz field is a correction to the macroscopic continuum model and attempts to account for the local microscopic distribution of moments. The slope of the measured phase difference versus echo time, as shown in Fig. 3.29(b), will yield δB_L. For cylindrical geometries, the induced fields are simply related to the susceptibility. For a long cylinder, the internal and external field distortions, are given by the following[73]:

Internal:

$$\delta B_L = \frac{\Delta\chi B_0}{6}(3\cos^2\theta - 1), \tag{3.25}$$

External:

$$\delta B_L = \frac{\Delta\chi B_0}{2}\frac{a^2}{r^2}\,\sin^2\theta\cos 2\phi, \tag{3.26}$$

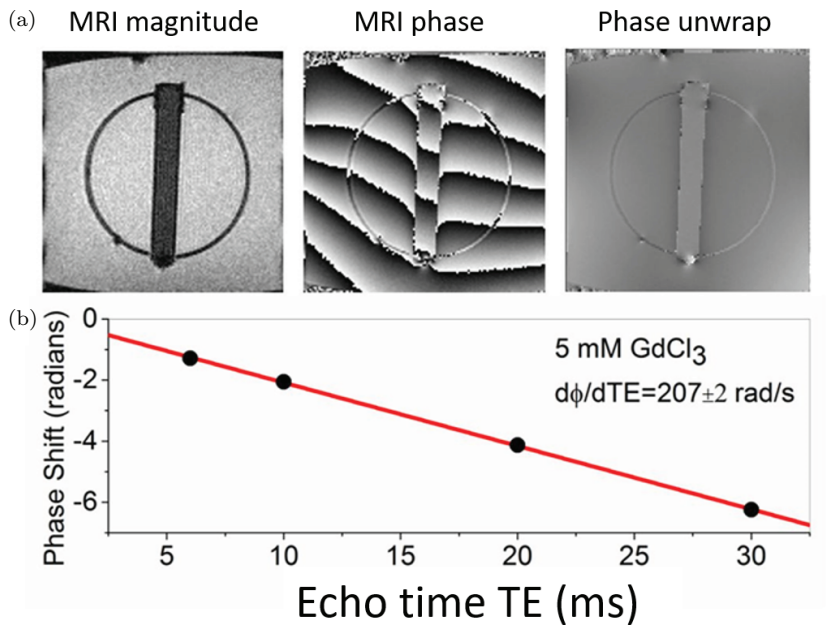

Fig. 3.29. (a) Magnitude and phase images of a vial containing 5.0 mM $GdCl_3$. The dark circle in the magnetic resonance amplitude image is a 76-mm diameter polycarbonate support for the vials. The third image shows the phase after unwrapping and after the long wavelength background has been subtracted. (b) Phase difference as a function of echo time (TE) taken from phase maps. From Ref. 72.

where $\Delta\chi$ is the susceptibility difference between the inside and outside of the cylinder, θ is the angle of the cylinder axis with respect to the main field, ϕ is the azimuthal angle of the observation point relative to the plane of the main field and cylinder axis, and a is the radius of the cylinder. Figure 3.30(a) shows measured field distortions for the phantom shown in Fig. 3.29(a) and compares with the prediction in the above equations, showing reasonable agreement.

For the simple case where the cylinder is aligned with the main field ($\theta = 0$), the susceptibility difference is given by $\Delta\chi = \frac{3\delta\phi}{\gamma_p B_0 TE}$. By measuring the slope of $\delta\phi$ versus TE, as shown in Fig. 3.29(b), the susceptibility can be determined. The susceptibility difference of the 5.0-mM $GdCl_3$ solution at 300 K using the data in Fig. 3.29(b) was $(1.55 \pm 0.02) \times 10^{-6}$, compared to the theoretical value of 1.65×10^{-6}, assuming a spin component of $s = 7/2$ and no orbital component.

The generated local fields and measured phase shifts are highly dependent on the orientation, as seen in Fig. 3.30(b). These data were obtained by rotating the vials of the paramagnetic salt solution inside the scanner. The

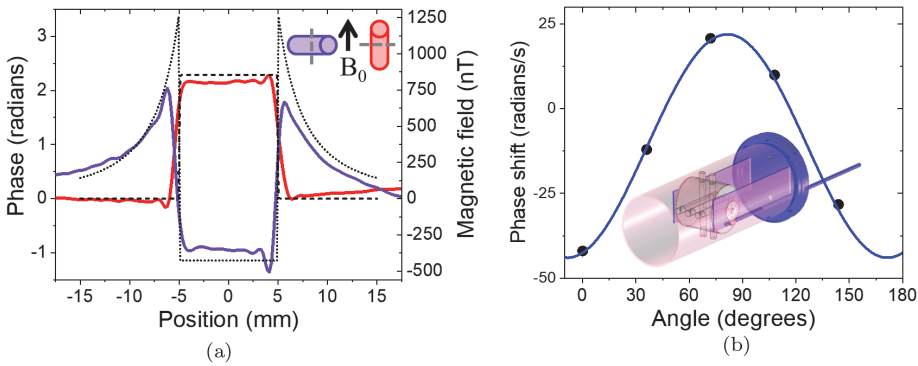

Fig. 3.30. (a) Measured phase shift and magnetic field distortion versus position for a phantom with a 5.0 mM $GdCl_3$ vial. The red and blue curves show data for B_0 parallel and perpendicular to the cylinder axis, respectively. Shown in the black are the theoretical predictions for the field distortion for ideal infinitely long cylinders. (b) The phase shift measured as a function of angle between B_0 and the cylinder axis, for a 1.0-mM-GdCl3 vial at 1.5 T, as the vial is rotated in the magnetic resonance imaging (MRI) bore. The inset shows a schematic of the rotating phantom structure. From Ref. 72.

angle-dependent data can be fit using Eq. (3.24) yielding $\Delta\chi = (3.24 \pm 0.05) \times 10^{-7}$ for a 1.0-mM $GdCl_3$ solution versus the theoretical value of 3.38×10^{-7} at 20°C.

Accurate susceptibility measurements in humans are considerably more complex. The magnetic field distortion is a convolution of the magnetic susceptibility distribution, $\chi(\mathbf{r})$, with the magnetic dipole kernel, $d(r)$:$\delta B_L(\mathbf{r}) = (\chi \otimes d)(\mathbf{r})$.[74] By Fourier transforming this equation, we get a simpler equation in k-space:

$$\chi(\mathbf{k}) = \frac{\delta B_L(\mathbf{k})}{d(\mathbf{k})}, \tag{3.27}$$

$$d(\mathbf{k}) = 1/3 - k_z^2/k^2. \tag{3.28}$$

The susceptibility map can be obtained by inverting the field profile, although complex methods are required since this inversion is not unique.[75–78] The nonuniqueness is because the dipole kernel, in k-space, has zeroes. Physically, this corresponds to the fact that for any given susceptibility distribution within a specified volume, arbitrary sources can be placed outside this volume and change the local fields but not the susceptibility distribution. When done properly, quantitative susceptibility maps can be made in humans with resolution below 0.1 ppm. Careful validation against primary phantoms is required to ensure the techniques used are robust and accurate.

Quantitative susceptibility mapping (QSM)[79] is increasingly used instead of qualitative techniques, such as susceptibility-weighted imaging,[80] to map neural diseases,[81–83] blood oxygen content,[84] and iron overload in the heart and liver.[85] Some neurodegenerative diseases, such as Parkinson's disease and Alzheimer's disease, have been associated with excess iron in the brain.[70,86] MRI has the unique ability to measure oxygen concentration of deep-lying vessels in the brain. A reproducible and quantitative method is important for finding and determining the severity of cerebral microbleeds resulting from traumatic brain injury. Measurements of iron overload in the heart and liver, caused by diseases such as hemochromatosis, are important because iron can catalyze the conversion of hydrogen peroxide into free radicals, causing damage to cell membranes, proteins, and DNA.[87]

3.6. B_1 Mapping, Measurement of EM Properties

The B_1 field intensity and phase will vary across a sample/patient due to nonuniformity of the transmit radiation pattern and to changing permittivity and conductivity of the tissues in patients, or materials in phantoms. RF power can be absorbed or reflected causing a VFA across the patient/phantom. Nonuniform B_1 can lead to artifacts and errors in qualitative MRI-based measurements or, alternatively, can be used as a method to map the EM properties of an object. Typical B_1 distortion can be seen in Fig. 3.31, which shows a flip angle map of the T_1 array on the NIST/ISMRM system phantom. These maps are required to correct for measurements such as T_1-VFA, in which the flip angles must be precisely determined. Various B_1 shimming methods are used to compensate for this variation to provide near-homogenous signal uniformity across the field of view.[88–90] This methodology is adequate for the qualitative imaging of the anatomy, but for the development of quantitative imaging biomarkers, correction of B_1 bias is necessary.

B_1 inhomogeneity is a large source of error in quantitative measurements with magnetization transfer (MT), specific absorption ratio (SAR), and quantitative T_1. B_1 inhomogeneity has been the focus of the RSNA-QIBA[22,91] dynamic contrast enhancement committee[g] and has also been noted as a significant obstacle for the magnetic resonance fingerprinting technique.

[g]The Radiological Society of North America (RSNA) has a dedicated set of committees as part of their Quantitative Imaging Biomarkers Alliance (QIBA) to promote accuracy and reproducibility in image-based biomarker measurements.

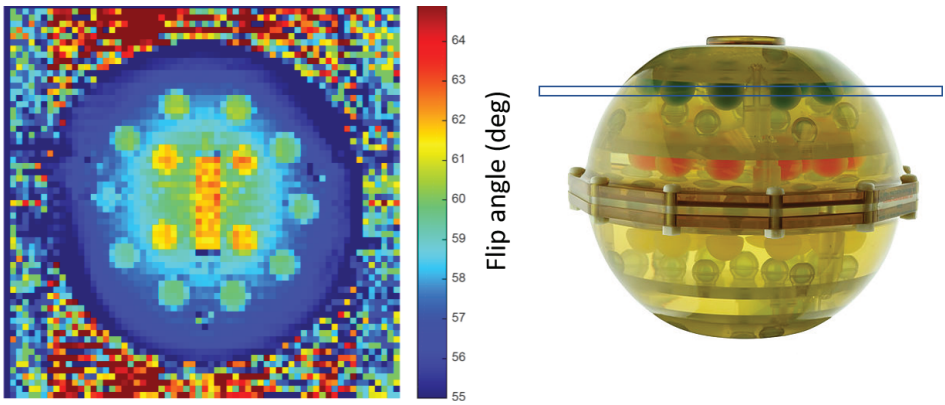

(a) (b)

Fig. 3.31. (a) Flip angle map of the National Institute of Standards and Technology (NIST)/International Society of Magnetic Resonance in Medicine (ISMRM) system phantom showing lower than prescribed flip angle, FA = 60°, near the periphery of the phantom. (b) Photo of the phantom with the image slice highlighted.

There are a variety of T_1 mapping methods that have been validated using phantoms, but they demonstrate up to 20% differences when applied to *in vivo* imaging.[92] The IR method for determining T_1 is widely considered to be the ground truth standard by which to compare other T_1 sequences and is used to measure the T_1 of the solutions in the NIST phantoms. However, as a clinical technique, the time to acquire IR image data is impractical. The VFA technique is widely adopted for its rapid data acquisition and for providing high resolution. VFA can be used to generate three-dimensional T_1 volumetric data; however, it is highly sensitive to B_1 inhomogeneity.[93] To improve the accuracy and precision of VFA, T_1 maps acquired at 3 T and higher field strengths, generation of B_1 maps, and bias correction are required.

There are a variety of methods to acquire image data to assess B_1 inhomogeneity,[94,95] and the accuracy of the flip angle achieved at any position depends on the inhomogeneity and can be determined by B_1 mapping. The calculation for B_1 inhomogeneity is usually straightforward. You can apply it to the VFA method to get a corrected T_1. When using fast-spoiled gradient echo,[96] B_1 inhomogeneity is related to the signal, repetition time, and T_1 through the VFA equation, modified to account for variation in the flip angle from the prescribed flip angle α:

$$S(\alpha) = S_{90} \sin(\zeta\alpha) \frac{1 - e^{-\frac{TR}{T_1}}}{1 - e^{-\frac{TR}{T_1}} \cos(\zeta\alpha)}. \tag{3.29}$$

Here, α is fixed and ζ is allowed to vary to obtain a position-dependent flip angle $\zeta\alpha$.

There are different approaches on how the T_1 value can be assessed, as the exact T_1 value is not known at this stage. A simple way is to use an assumed constant T_1, which should preferably be in the same range as the expected T_1 of the investigated object. The effect of using such an assumption is evaluated with phantom measurements.

The major problem is to obtain an accurate spatial *in vivo* B_1 map with a B_1 mapping sequence.[97] The double angle method is the most accurate but also the slowest.[98] This usually limits its usage to organs not affected by the respiratory motion and nonclinical protocols. More popular techniques are the Bloch–Siegert shift method and actual flip angle imaging. Both are faster methods to obtain B_1 maps.

If accurate B_1 maps can be obtained, they can be used to measure the EM properties, relative permittivity ε_{r}, and conductivity σ of the sample/patient. The field propagation, at a frequency ω into a complex media, is governed by[99]

$$-\nabla^2\mathbf{H} = \omega^2\mu_0\epsilon_c\mathbf{H} + (\boldsymbol{\nabla}\epsilon_c/\epsilon_c) \times (\boldsymbol{\nabla} \times \mathbf{H}), \tag{3.30}$$

where $\epsilon_c = \epsilon_r\epsilon_0 - i\sigma/\omega$. If the EM properties are locally homogenous, the equation can be simplified to give a Helmholtz equation governing the spatial distribution of the transmit RF field $H_1^+ = (B_{1x} + iB_{1y})/2\mu_0$:

$$-\nabla^2 H_1^+ = \omega^2\mu_0\epsilon_c H_1^+. \tag{3.31}$$

The transmit RF field can be mapped using MRI and Eq. (3.30) can be inverted to give a spatial map of the EM properties. New EM mapping techniques using MRI, such as magnetic resonance electrical property tomography, can be used to map EM properties at the Larmor frequency of the MRI system.[100,101] Other techniques, such as magnetic resonance electrical impedance tomography, can measure low-frequency conductivity (DC to 1 kHz) by using MRI to sense the field created by injected currents. Given the complexity and heterogeneity of the tissue, these techniques need to be carefully validated before being used for disease studies or clinical applications.

3.7. Summary

Here, we have discussed how MRI can be used as an RF probe to make quantitative measurements and maps inside objects such as the human body. Nuclear spin probes, excited and detected by RF radiation, can be used

to measure many different important parameters within the human body. Careful development and validation of imaging sequences are required to make MRI a precise metrology suitable for clinical decisions. The use of primary calibration structures, such as NIST-traceable phantoms, is essential to determine the accuracy and reproducibility of MRI-based measurements. For most applications, several reliable and precisely determined biomarkers may be required to determine tissue type and disease state. Newer techniques, capable of accurate simultaneous measurement of several important parameters,[18,71,102] hold great promise in advancing medical imaging into a precise *in vivo* metrology.

References

1. R. W. Brown, Y.-C. N. Cheng, E. M. Haacke, M. R. Thompson, and R. Venkatesan, *Magnetic Resonance Imaging: Physical Principles and Sequence Design*. (John Wiley & Sons, Inc., Hoboken, New Jersey, 2014).
2. D. G. Mitchell and M. P. D. Cohen, *MRI Principles*, 2nd edn. (Saunders, Philadelphia, 2004).
3. V. Kuperman, *Magnetic Resonance Imaging: Physical Principles and Applications* (Elsevier Science, 2000).
4. B. W. Petley and R. W. Donaldson, The temperature dependence of the diamagnetic shielding correction for proton NMR in water, *Metrologia*. **20**, 81 (1984).
5. V. Jain, O. Abdulmalik, K. J. Propert, and F. W. Wehrli, Investigating the magnetic susceptibility properties of fresh human blood for noninvasive oxygen saturation quantification, *Magn. Reson. Med.: Official Journal of the Society of Magnetic Resonance in Medicine/Society of Magnetic Resonance in Medicine* **68**, 863–867 (2012).
6. N. Bloembergen and R. V. Pound, Radiation damping in magnetic resonance experiments, *Phys. Rev.* **95**, 8–12 (1954).
7. S. Tofts Paul, PD: Proton density of tissue water, in *Quantitative MRI of the Brain*, Ch. 4 (Wiley Online Books, 2004), pp. 83–103. doi: 10.1002/0470869526.ch4.
8. J. Z. Bojorquez *et al.*, What are normal relaxation times of tissues at 3T? *Magn. Reson. Imag.* **35**, 69–80 (2017).
9. G. J. Stanisz *et al.*, T1, T2 relaxation and magnetization transfer in tissue at 3T, *Magn. Reson. Med: Official Journal of the Society of Magnetic Resonance in Medicine/Society of Magnetic Resonance in Medicine*. **54**, 507–512 (2005).
10. G. E. Gold *et al.*,Musculoskeletal MRI at 3.0 T: Relaxation times and image contrast, *Am. J. Roentgenol.* **183**, 343–351 (2004).
11. R. Rakow-Penner, B. Daniel, H. Yu, A. Sawyer-Glover, and G. H. Glover, Relaxation times of breast tissue at 1.5T and 3T measured using IDEAL, *J. Magnet. Reson. Imag.* **23**, 87–91 (2006).
12. R. A. Edden, S. A. Smith, and P. B. Barker, Longitudinal and multi-echo transverse relaxation times of normal breast tissue at 3 Tesla, *J. Magnet. Reson. Imag.* **32**, 982–987 (2010).
13. J. Du *et al.*, Qualitative and quantitative ultrashort echo time (UTE) imaging of cortical bone, *J. Magn. Reson.* **207**, 304–311 (2010).
14. P. Schmitt *et al.*, Inversion recovery TrueFISP: Quantification of T(1), T(2), and spin density, *Magn. Reson. Med.: Official Journal of the Society of Magnetic Resonance in Medicine/Society of Magnetic Resonance in Medicine*. **51**, 661–667 (2004).

15. H. Lu *et al.*, Routine clinical brain MRI sequences for use at 3.0 Tesla, *J. Magn. Reson. Imag.* **22**, 13–22 (2005).
16. W. Shin, H. Gu, and Y. Yang, Fast high-resolution $T1$ mapping using inversion recovery. Look-Locker echo-planar imaging at steady state: Optimization for accuracy and reliability, *Magn. Reson. Med.: Official Journal of the Society of Magnetic Resonance in Medicine/Society of Magnetic Resonance in Medicine.* **61**, 899–906 (2009).
17. S. Gutteridge, C. Ramanathan, and R. Bowtell, Mapping the absolute value of M0 using dipolar field effects, *Magn. Reson. Med: Official Journal of the Society of Magnetic Resonance in Medicine/Society of Magnetic Resonance in Medicine.* **47**, 871–879 (2002).
18. W. Krauss, M. Gunnarsson, T. Andersson, and P. Thunberg, Accuracy and reproducibility of a quantitative magnetic resonance imaging method for concurrent measurements of tissue relaxation times and proton density, *Magn. Reson. Imag.* **33**, 584–591 (2015).
19. Y. Jiang, D. Ma, N. Seiberlich, V. Gulani, and A. Griswold Mark, MR fingerprinting using fast imaging with steady state precession (FISP) with spiral readout, *Magn. Reson. Med.* **74**, 1621–1631 (2014).
20. C. M. J. de Bazelaire, G. D. Duhamel, N. M. Rofsky, and D. C. Alsop, MR imaging relaxation times of abdominal and pelvic tissues measured *in vivo* at 3.0 T: Preliminary results, *Radiology.* **230**, 652–659 (2004).
21. F. von Knobelsdorff-Brenkenhoff *et al.*, Myocardial T(1) and T(2) mapping at 3 T: Reference values, influencing factors and implications, *J. Cardiovasc. Magn. Reson.* **15**, 53–53 (2013).
22. L. G. Kessler *et al.*, The emerging science of quantitative imaging biomarkers terminology and definitions for scientific studies and regulatory submissions, *Stat. Methods Med. Res.* **24**(1), 9–26 (2015).
23. A. Abragam, *Principles of Nuclear Magnetism* (*International Series of Monographs on Physics*) (Oxford University Press, USA, 1983).
24. H. Benoit-Cattin, G. Collewet, B. Belaroussi, H. Saint-Jalmes, and C. Odet, The SIMRI project: A versatile and interactive MRI simulator, *J. Magn. Reson.* **173**, 97–115 (2005).
25. R. Kose and K. Kose, BlochSolver: A GPU-optimized fast 3D MRI simulator for experimentally compatible pulse sequences, *J. Magn. Reson.* **281**, 51–65 (2017).
26. P. Shkarin and R. G. S. Spencer, Direct simulation of spin echoes by summation of isochromats, *Concepts Magn. Reson.* **8**, 253–268 (1996).
27. R. R. Ernst and W. A. Anderson, Application of fourier transform spectroscopy to magnetic resonance, *Rev. Sci. Instrum.* **37**, 93–102 (1966).
28. M. H. Levitt, Composite pulses, *Prog. Nucl. Magn. Reson. Spectrosc.* **18**, 61–122 (1986).
29. S. Meiboom and D. Gill, Modified spin-echo method for measuring nuclear relaxation times, *Rev. Sci. Instrum.* **29**, 688–691 (1958).
30. J. Pauly, P. Le Roux, D. Nishimura, and A. Macovski, Parameter relations for the Shinnar-Le Roux selective excitation pulse design algorithm [NMR imaging], *IEEE Trans. Med. Imag.* **10**, 53–65 (1991).
31. NEMA, *MS 5 Determination of Slice Thickness in Diagnostic Magnetic Resonance Imaging* (National Electrical Manufacturers Association, 2010).
32. B. Zhu, J. Z. Liu, S. F. Cauley, B. R. Rosen, and M. S. Rosen, Image reconstruction by domain-transform manifold learning, *Nature.* **555**, 487–492 (2018).
33. J. Mispelter, M. Lupu, and A. Briguet, *NMR Probeheads For Biophysical and Biomedical Experiments* (Imperial College Press, London, 2015).

34. C. E. Hayes, W. A. Edelstein, J. F. Schenck, O. M. Mueller, and M. Eash, An efficient, highly homogeneous radiofrequency coil for whole-body NMR imaging at 1.5 T, *J. Magn. Reson.* **63**, 622–628 (1985).
35. J. Jin, *Electromagnetic Analysis and Design in Magnetic Resonance Imaging* (CRC Press, Boca Raton, FL, 1998).
36. C. L. Chin, C. M. Collins, S. Li, B. J. Dardzinski, and M. B. Smith, BirdcageBuilder: Design of specified-geometry birdcage coils with desired current pattern and resonant frequency, *Concepts Magn. Reson.* **15**, 156–163 (2002).
37. J. R. Corea *et al.*, Screen-printed flexible MRI receive coils, *Nat. Commun.* **7**, 10839 (2016).
38. P. Glover and R. Bowtell, MRI rides the wave, *Nature.* **457**, 971 (2009).
39. D. O. Brunner, N. De Zanche, J. Fröhlich, J. Paska, and K. P. Pruessmann, Travelling-wave nuclear magnetic resonance, *Nature.* **457**, 994 (2009).
40. X. Yan, X. Zhang, J. C. Gore, and W. A. Grissom, Improved traveling-wave efficiency in 7T human MRI using passive local loop and dipole arrays, *Magn. Reson. Imag.* **39**, 103–109 (2017).
41. E. Keenan Kathryn *et al.*, Quantitative magnetic resonance imaging phantoms: A review and the need for a system phantom, *Magn. Reson. Med.* **79**, 48–61 (2017).
42. J. L. Gunter *et al.*, Measurement of MRI scanner performance with the ADNI phantom, *Med. Phys.* **36**, 2193–2205 (2009).
43. K. E. Keenan *et al.*, Design of a breast phantom for quantitative MRI, *J. Magn. Reson. Imag.* **44**, 610–619 (2016).
44. K. E. Keenan *et al.*, Variability and bias assessment in breast ADC measurement across multiple systems, *J. Magn. Reson. Imag.* **44**, 846–855 (ACR MRI Accreditation Program, 2016).
45. The American College of Radiology 1891 Preston White Dr Reston, VA 20191–4397.
46. T. M. Ihalainen *et al.*, MRI quality assurance using the ACR phantom in a multi-unit imaging center, *Acta Oncol.* **50**, 966–972 (2011).
47. J. M. Kowalewski, *Nuclear Spin Relaxation in Liquids: Theory, Experiments, and Applications*, Vol. 2, Series in Chemical Physics (Taylor & Francis, New York, 2006).
48. P. B. Kingsley, Methods of measuring spin-lattice ($T1$) relaxation times: An annotated bibliography, *Concepts Magn. Reson.* **11**, 243–276 (1999).
49. R. L. Vold, R. R. Vold, and H. E. Simon, Errors in measurements of transverse relaxation rates, *J. Magn. Reson.* **11**, 283–298 (1973).
50. S. Majumdar, S. C. Orphanoudakis, A. Gmitro, M. O'Donnell, and J. C. Gore, Errors in the measurements of T2 using multiple-echo MRI techniques I. Effects of radiofrequency pulse imperfections, *Magn. Reson. Med.* **3**, 397–417 (1986).
51. S. Majumdar, S. C. Orphanoudakis, A. Gmitro, M. O'Donnell, and J. C. Gore, Errors in the measurements of T2 using multiple-echo MRI techniques II. Effects of static field inhomogeneity, *Magn. Reson. Med.* **3**, 562–574 (1986).
52. B. R. Condon, J. Patterson, D. Wyper, A. Jenkins, and D. M. Hadley, Image nonuniformity in magnetic resonance imaging: Its magnitude and methods for its correction, *Br. J. Radiol.* **60**, 83–87 (1987).
53. R. A. Lerski, Multi-center trial with protocols and prototype test objects for the assessment of MRI equipment, *Magn. Reson. Imag.* **6**, 201–214 (1988).
54. E. A. Vokurka, N. A. Thacker, and A. Jackson, A fast model independent method for automatic correction of intensity nonuniformity in MRI data, *J. Magn. Reson. Imag.* **10**, 550–562 (1999).
55. J. M. Pope and N. Repin, A simple approach to T2 imaging in MRI, *Magn. Reson. Imag.* **6**, 641–646 (1988).

56. J. Henning, Multiecho imaging sequences with low refocusing flip angles, *J. Magn. Reson.* **78**, 397–407 (1988).
57. A. P. Crawley and R. M. Henkelman, Errors in T2 estimation using multislice multiple-echo imaging, *Magn. Reson. Med.* **4**, 34–47 (1987).
58. D. A. G. Wicks, G. J. Barker, and P. S. Tofts, Correction of intensity nonuniformity in MR images of any orientation, *Magn. Reson. Imag.* **11**, 183–196 (1993).
59. R. M. Lebel and A. H. Wilman, Transverse relaxometry with stimulated echo compensation, *Magn. Reson. Med.* **64**, 1005–1014 (2010).
60. J.-M. Bonny, M. Zanca, J.-Y. Boire, and A. Veyre, T2 maximum likelihood estimation from multiple spin-echo magnitude images, *Magn. Reson. Med.* **36**, 287–293 (1996).
61. W. D. Foltz, J. A. Stainsby, and G. A. Wright, T2 accuracy on a whole-body imager, *Magn. Reson. Med.* **38**, 759–768 (1997).
62. Y. DeDeene, D. DeWagter, W. DeNeve, and E. Achten, Artefacts in multi-echo T2 imaging for high precision gel dosimetry: II. Analysis of B1-field inhomogeneity, *Phys. Med. Biol.* **45**, 1825–1839 (2000).
63. J. G. Sled and G. B. Pike, Correction for B1 and B0 variations in quantitative T2 measurements using MRI, *Magn. Reson. Med.* **43**, 589–593 (2000).
64. M. Lepage, P. S. Tofts, S. A. J. Back, P. M. Jayasekera, and C. Baldock, Simple methods for the correction of T2 maps of phantoms, *Magn. Reson. Med.* **46**, 1123–1129 (2001).
65. G. S. Pell, R. S. Briellmann, A. B. Waites, D. F. Abbott, D. P. Lewis, and G. D. Jackson, Optimized clinical T2 relaxometry with a standard CPMG sequence, *J. Magn. Reson. Imag.* **23**, 248–252 (2006).
66. S. W. Anderson, O. Sakai, J. A. Soto, and H. Jara, Improved T2 mapping accuracy with dual-echo tubo spin echo: Effect of phase encoding profile orders, *Magn. Reson. Med.* **69**, 137–143 (2013).
67. A. Simmons, P. S. Tofts, G. J. Barker, and S. R. Arridge, Sources of intensity nonuniformity in spin echo images at 1.5 T, *Magn. Reson. Med.* **32**, 121–128 (1994).
68. R. V. Mulkern, S. T. S. Wong, P. Jakab, A. R. Bleier, T. Sandor, and F. A. Jolesz, CPMG imaging sequences for high field *in vivo* transverse relaxation studies, *Magn. Reson. Med.* **16**, 67–79 (1990).
69. R. R. Edelman, The history of MR imaging as seen through the pages of radiology, *Radiology* **273**, S181–S200 (2014).
70. F. Mitsumori, H. Watanabe, and N. Takaya, Estimation of brain iron concentration *in vivo* using a linear relationship between regional iron and apparent transverse relaxation rate of the tissue water at 4.7 T, *Magn. Reson. Med.: Official Journal of the Society of Magnetic Resonance in Medicine/Society of Magnetic Resonance in Medicine* **62**, 1326–1330 (2009).
71. D. Ma *et al.*, Magnetic resonance fingerprinting, *Nature* **495**, 187–192 (2013).
72. H. E. Erdevig, S. E. Russek, S. Carnicka, K. F. Stupic, and K. E. Keenan, Accuracy of magnetic resonance based susceptibility measurements, *AIP Adv.* **7**, 056718 (2017).
73. J. Neelavalli and Y.-C. N. Cheng, *Susceptibility Weighted Imaging in MRI* (John Wiley and Sons, Inc., Hoboken, NJ, 2011), pp. 17–31.
74. F. Schweser, A. Deistung, B.W. Lehr, and J. R. Reichenbach, Differentiation between diamagnetic and paramagnetic cerebral lesions based on magnetic susceptibility mapping, *Med. Phys.* **37**, 5165–5178 (2010).
75. T. Liu *et al.*, Morphology enabled dipole inversion (MEDI) from a single-angle acquisition: Comparison with COSMOS in human brain imaging, *Magn. Reson. Med: Official Journal of the Society of Magnetic Resonance in Medicine/Society of Magnetic Resonance in Medicine* **66**, 777–783 (2011).

76. L. de Rochefort, R. Brown, M. R. Prince, and Y. Wang, Quantitative MR susceptibility mapping using piece-wise constant regularized inversion of the magnetic field, *Magn. Reson. Med: Official Journal of the Society of Magnetic Resonance in Medicine/Society of Magnetic Resonance in Medicine* **60**, 1003–1009 (2008).
77. T. Liu, P. Spincemaille, L. de Rochefort, B. Kressler, and Y. Wang, Calculation of susceptibility through multiple orientation sampling (COSMOS): A method for conditioning the inverse problem from measured magnetic field map to susceptibility source image in MRI, *Magn. Reson. Med: Official Journal of the Society of Magnetic Resonance in Medicine/Society of Magnetic Resonance in Medicine* **61**, 196–204 (2009).
78. Y. C. Cheng, J. Neelavalli, and E. M. Haacke, Limitations of calculating field distributions and magnetic susceptibilities in MRI using a Fourier based method, *Phys. Med. Biol.* **54**, 1169–1189 (2009).
79. Y. Wang and T. Liu, Quantitative susceptibility mapping (QSM): Decoding MRI data for a tissue magnetic biomarker, *Magn. Reson. Med: Official Journal of the Society of Magnetic Resonance in Medicine/Society of Magnetic Resonance in Medicine* **73**, 82–101 (2015).
80. E. M. Haacke, S. Mittal, Z. Wu, J. Neelavalli, and Y. C. Cheng, Susceptibility weighted imaging: Technical aspects and clinical applications, part 1, *AJNR. Am. J. Neuroradiol.* **30**, 19–30 (2009).
81. J. H. Jensen *et al.*, Magnetic field correlation as a measure of iron-generated magnetic field inhomogeneities in the brain, *Magn. Reson. Med.: Official Journal of the Society of Magnetic Resonance in Medicine/Society of Magnetic Resonance in Medicine* **61**, 481–485 (2009).
82. K. Shmueli *et al.*, Magnetic susceptibility mapping of brain tissue in vivo using MRI phase data, *Magn. Reson. in Med: Official Journal of the Society of Magnetic Resonance in Medicine/Society of Magnetic Resonance in Medicine* **62**, 1510–1522 (2009).
83. H. Tan *et al.*, Evaluation of iron content in human cerebral cavernous malformation using quantitative susceptibility mapping, *Invest. Radiol.* **49**, 498–504 (2014).
84. E. M. Haacke, K. Prabhakaran, I. R. Elangovan, Z. Wu, and J. Neelavalli, *Susceptibility Weighted Imaging in MRI* (John Wiley & Sons, Inc., 2011), pp. 517–528.
85. S. D. Sharma, D. Hernando, D. E. Horng, and S. B. Reeder, Quantitative susceptibility mapping in the abdomen as an imaging biomarker of hepatic iron overload, *Magn. Reson. Med.* **74**, 673–683 (2015).
86. S. Oshiro, M. S. Morioka, and M. Kikuchi, Dysregulation of iron metabolism in Alzheimer's disease, Parkinson's disease, and amyotrophic lateral sclerosis, *Adv. Pharmacol. Sci.* **2011**, 378278 (2011).
87. N. C. Andrews, Disorders of iron metabolism, *New Eng. J. Med.* **341**, 1986–1995 (1999).
88. G. Adriany *et al.*, Transmit and receive transmission line arrays for 7 Tesla parallel imaging, *Magn. Reson. Med: Official Journal of the Society of Magnetic Resonance in Medicine/Society of Magnetic Resonance in Medicine* **53**, 434–445 (2005).
89. C. M. Collins, W. Liu, B. J. Swift, and M. B. Smith, Combination of optimized transmit arrays and some receive array reconstruction methods can yield homogeneous images at very high frequencies, *Magn. Reson. Med.* **54** (2005).
90. S. B. King, R. Duensing, S. Varosi, D. Peterson, and D. A. Molyneaux, A four channel transceive phased array head coil for 3T, in *Proc. 9th Int. Soc. Magn. Reson. Med. Glasgow* (2001) Scotland, UK, p. 12.

91. D. L. Raunig *et al.*, Quantitative imaging biomarkers: A review of statistical methods for technical performance assessment, *Statist. Meth. Med. Res.* **24**, 27–67 (2014).
92. N. Stikov *et al.*, On the accuracy of $T1$ mapping: Searching for common ground, *Magn. Reson. Med.* **73**, 514–522 (2015).
93. J. G. Sled and G. B. Pike, Standing-wave and RF penetration artifacts caused by elliptic geometry: An electrodynamic analysis of MRI, *IEEE Trans. Med. Imag.* **17**, 653–662 (1998).
94. K. Sung, L. Daniel Bruce, and A. Hargreaves Brian, Transmit field inhomogeneity and $T1$ estimation errors in breast DCE-MRI at 3 tesla, *J. Magn. Reson. Imag.* **38**, 454–459 (2013).
95. J. J. van Schie, C. Lavini, L. J. van Vliet, and F. M. Vos, Feasibility of a fast method for B1-inhomogeneity correction for FSPGR sequences, *Magn. Reson. Imag.* **33**, 312–318 (2015).
96. R. J. Fram *et al.*, Rapid calculation of $T1$ using variable flip angle gradient refocused imaging, *Magn. Reson. Imag.* **5**(3), 201–208 (1987).
97. A. Lutti, C. Hutton, J. Finsterbusch, G. Helms, and N. Weiskopf, Optimization and validation of methods for mapping of the radiofrequency transmit field at 3T, *Magn. Reson. Med: Official Journal of the Society of Magnetic Resonance in Medicine/Society of Magnetic Resonance in Medicine* **64**, 229–238 (2010).
98. W. P. Stollberger, R. McKinnon, G. Justich, and E. Ebner, Rf-field mapping *in vivo*, in *Proc. 7th Ann. Meeting of SMRM*, San Francisco, CA, USA, p. 106 (1988).
99. X. Zhang, J. Liu, and B. He, Magnetic-resonance-based electrical properties tomography: A review, *IEEE Rev. Biomed. Eng.* **7**, 87–96 (2014).
100. S. Jin Keun *et al.*, Electrical tissue property imaging using MRI at dc and Larmor frequency, *Inverse Probl.* **28**, 084002 (2012).
101. F. S. Hafalir, O. F. Oran, N. Gurler, and Y. Z. Ider, Convection-reaction equation based magnetic resonance electrical properties tomography (cr-MREPT), *IEEE Trans. Med. Imag.* **33**, 777–793 (2014).
102. J. B. Warntjes, O. D. Leinhard, J. West, and P. Lundberg, Rapid magnetic resonance quantification on the brain: Optimization for clinical usage, *Magn. Reson. Med: Official Journal of the Society of Magnetic Resonance in Medicine/Society of Magnetic Resonance in Medicine* **60**, 320–329 (2008).